The Sensitivity of Simulated Storm Structure, Intensity, and Precipitation Efficiency to Environmental Temperature

EUGENE W. MCCAUL JR. AND CHARLES COHEN

Universities Space Research Association, Huntsville, Alabama

CODY KIRKPATRICK

University of Alabama in Huntsville, Huntsville, Alabama

(Manuscript received 13 July 2004, in final form 1 April 2005)

ABSTRACT

Prior parameter space studies of simulated deep convection are extended to embrace shifts in the environmental temperature. Within the context of the parameter space study design, shifts in this environmental temperature are roughly equivalent to changes in the ambient precipitable water (PW). Two series of simulations are conducted: one in a warm environmental regime that is associated with approximately 60 mm of precipitable water, and another with temperatures 8°C cooler, so that PW is reduced to roughly 30 mm. The sets of simulations include tests of the impact of changes in the buoyancy and shear profile shapes and of changes in mixed- and moist layer depths, all of which have been shown to be important in prior work. Simulations discussed here also feature values of surface-based pseudoadiabatic convective available potential energy (CAPE) of 800, 2000, or 3200 J kg^{-1}, and a single semicircular hodograph having a radius of 12 m s^{-1}, but with variable vertical shear.

The simulations reveal a consistent trend toward stronger peak updraft speeds for the cooler temperature (reduced PW) cases, when the other environmental parameters are held constant. Roughly comparable increases in updraft speeds are noted for all combinations of mixed- and moist layer depths. These increases in updraft strength evidently result from both the reduction of condensate loading aloft and the lower altitudes at which the latent heat release by freezing and deposition commences in the cooler, low-PW environments. As expected, maximum storm precipitation rates tend to diminish as PW is decreased, but only slightly, and by amounts not proportionate to the decrease in PW. The low-PW cases thus actually feature larger environment-relative precipitation efficiency than do the high-PW cases. In addition, more hail reaches the surface in the low-PW cases because of reduced melting in the cooler environments. Although these experiments were designed to feature specified amounts of pseudoadiabatic CAPE, it appears that reversible CAPE provides a more accurate prediction of updraft strength, at least for the storms discussed here.

1. Introduction

In early parameter space studies of simulated convective storms, Weisman and Klemp (1982, 1984) demonstrated the importance of bulk convective available potential energy (CAPE) and vertical shear on storm morphology and intensity. Later, McCaul and Weisman (2001, hereafter MW01) devised a more general method of prescribing idealized starting environmental profiles, and showed that variations in the shapes of buoyancy and shear profiles also exerted a profound influence on storm behavior. In CAPE-starved environments, storms were generally weak, except when the parcel buoyancy profile was shaped to provide a maximum close to cloud base, while in shear-starved environments, storms could become stronger if buoyancy reached a maximum at higher altitudes, so that storm cold pools did not become too strong.

Subsequently, McCaul and Cohen (2002, hereafter MC02) extended the MW01 methodology to experiments using a cloud model that included the effects of ice microphysics, and explored the impact of variations in mixed and moist layer depths on storms. They also

Corresponding author address: Eugene W. McCaul Jr., Universities Space Research Association, 6700 Odyssey Dr., Suite 203, Huntsville, AL 35806.
E-mail: mccaul@space.hsv.usra.edu

proposed an expanded eight-dimensional parameter space that should embrace most of the significant sensitivities of convective storms to the vertical structure of their environments. MC02 found that storm cold pools became stronger as mixed-layer depth [related to the altitude of the lifted condensation level (LCL)] increased, and that updrafts experienced less dilution and were more intense as the moist layer depth [linked to the level of free convection (LFC)] increased. Other theoretical and observational support for the MC02 findings has come from Williams and Stanfill (2002), who invoked boundary layer similarity arguments to conclude that the warmer, drier boundary layers over land lead to larger, stronger updrafts that produce, as observations indicate, more lightning than maritime updrafts.

All the MW01 and MC02 simulation results were valid only for environments having very warm, moist subcloud layers (they specified an equivalent potential temperature $\theta_e = 354.3$ K there), with total precipitable water (PW) values near 60 mm. However, as pointed out by MC02, one of the eight parameters that describe the storm environment is the temperature at the LCL, T_L. The importance of this parameter has also been recognized by others (see, e.g., Cotton and Anthes 1989, 5–6). Thus, a proper parameter space study of convective storm morphology must include experiments having diverse values of T_L. If one decreases T_L while using the method of MW01 to specify an environmental temperature profile aloft, one obtains a new environmental profile having cooler temperatures aloft and, because the saturation vapor pressure grows exponentially with temperature, smaller amounts of environmental PW. Because the earlier experiments reported in MW01 and MC02 utilized values of T_L that implied PW values near the upper end of the observed distribution, it was decided to add new simulation experiments featuring cooler, lower-PW environments. By decreasing T_L by 8.0°C, we obtained environmental profiles with PW halved to approximately 30 mm. In the parameter space envisioned by MC02, however, the various PW values obtained for a given choice of T_L are only approximately equal to one another, because there is some small modulation of PW related to variations in some of the other key environmental parameters, namely, the shape of the parcel buoyancy profile and the altitudes of the LCL and LFC. While the original PW of about 60 mm corresponds to very moist tropical conditions, the new PW of about 30 mm corresponds to cooler, midlatitude convective conditions, such as those encountered regularly on the western Great Plains of the United States. Thus, we are able to specify idealized starting profiles for strongly contrasting pairs of numerical simulation experiments where all eight environmental parameters are the same except for T_L and its proxy, PW.

It is not entirely clear how storm intensity and morphology will vary as T_L and PW vary, all other factors being held constant. As Cotton and Anthes (1989) point out, larger T_L and PW imply greater potential for production of heavy precipitation. However, in the real atmosphere, large T_L and PW are often incidentally associated with relatively large CAPE. Within the parameter space framework of MC02, pseudoadiabatic surface-based CAPE (SBCAPE-P) is one of the key environmental parameters, and can be fully controlled for in the numerical simulation experiments. Under these controls, any SBCAPE-P-based advantage accruing to the high T_L, high-PW environments is eliminated. We are then left with the negative impact on buoyancy of the condensate loading. There are two alternative methods of treating this condensate loading: under the assumption of pseudoadiabatic ascent, all condensate promptly falls out and loading may be neglected; under the assumption of reversible ascent, all the condensate remains with the parcel. In the latter case, the condensate loading in the parcel may be theoretically estimated and used to make quantitative, downward-revised estimates of CAPE. Surface-based reversible CAPE (SBCAPE-RL) is defined here to include only the negative buoyancy effects of condensate loading, along with the smaller positive effects of the heat content of the condensate. If SBCAPE-RL is found to be more accurate than SBCAPE-P in describing our simulated storms, then we should expect the low T_L, low-PW storms to be stronger than those at high T_L and high PW, because of the former's larger values of SBCAPE-RL. In nature and in these simulations, however, the actual amounts of condensate loading are variable, and lie somewhere between the zero loading assumed in SBCAPE-P calculations and the often significant loading assumed in SBCAPE-RL calculations. The reversible theory might also be questioned because of its prediction that the maximum condensate loading occurs at the updraft summit, which is strongly at variance with what is found in observations and detailed simulations of storms.

SBCAPE-P, as calculated in ordinary meteorological operations and in these experiments, accounts only for the heat released by condensation processes. It does not account for the warming realized during the release of the latent heat of fusion. SBCAPE-RL computations, however, can be extended to include these effects; when we reference such CAPE computations herein, we denote this surface-based reversible CAPE with fusion as SBCAPE-RLF. In our computation of

SBCAPE-RLF, we include not only the freezing of preexisting hydrometeors, but also the ongoing process of deposition, and also the heat content of the hydrometeors. The effect of the heat of fusion on CAPE is positive, and can, in bulk, be comparable to that of the condensate loading, although the vertical distributions of the buoyancy contributions associated with the loading and fusion heating generally differ. Many authors have noted the tendency for bulk (full tropospheric) SBCAPE-RLF to resemble bulk SBCAPE-P, but we suspect that the differences in the vertical distributions of the effective buoyancies within the calculations are important, and might cause one method to be better at predicting updraft speeds than the other.

To further complicate the picture, the computation of SBCAPE-RLF requires an assumption to be made regarding the temperature at which the preexisting hydrometeors freeze. Williams and Renno (1993) assume that the freezing occurs at −10°C, while Emanuel (1994, chapter 14) uses 0°C. Other authors (Manzato and Morgan 2003; Li et al. 2004) assume the freezing occurs gradually between two prespecified temperatures. Although our model results indicate that freezing occurs in a distributed manner, with multiple peaks of fusional heat release, it is impractical to pursue SBCAPE-RLF calculations that attempt to account for behavior as complex as that seen in our simulation results. Thus, in our SBCAPE-RLF calculations, we assume hydrometeor freezing occurs at the −10°C temperature employed by Williams and Renno.

How then might the fusion heating itself affect our simulated storms? In the high T_L, high-PW environments, more water vapor is present, and the quantitative rates of fusion heating are greater than in the corresponding low T_L, low-PW environments. This fact suggests an advantage for the storms in the high-PW environments. However, the fusion warming occurs through a deeper layer of the troposphere in the low-PW environments, because of the greater proximity of cloud base to the freezing level there, and this could provide a significant boost to updraft energy in those environments. The possibility of updraft invigoration by fusion heating in low-PW environments also suggests that greater-than-expected amounts of precipitation might form there, which would tend to counteract the previously mentioned tendency for higher-PW environments to generate larger amounts of precipitation. In addition, whenever stronger updrafts occur, greater amounts of condensate loading are also likely, which provide a negative feedback that tends to restrain updraft strength and overall storm intensity.

Detailed observations or numerical simulations can help to sort out all the abovementioned complexities. Obtaining good observations is difficult, however, and it is almost impossible to gather enough data to be able to stratify in eight dimensions without suffering severe sampling problems and uncertainty related to observational error and unrepresentativeness. We thus turn to numerical simulations for guidance.

The purpose of this paper, therefore, is to present the results of numerical simulations that show, within the limitations of current modeling capabilities, what happens to storms in environments having different values of T_L and PW, all other key parameters being held constant across pairs of experiments being compared. We shall show that, on balance, storm updrafts do indeed tend to be stronger in the low T_L environments, consistent with their generally reduced condensate loading and their deeper layer affected by the release of the latent heat of fusion. These stronger updrafts at low PW are also associated with enhanced precipitation efficiency relative to the environmental PW and enhanced surface hail fall rates, but not outright actual total precipitation rates. In our diagnosis of updraft behavior, we also find that there are advantages to using the reversible CAPE theory as a means of explaining updraft strength.

This paper is organized in five main sections. Following this introduction, section 2 contains a description of the cloud model used in the experiments, and explains how the experiments are designed and conducted. Section 3 contains results, while section 4 features a discussion of the simulation findings. Section 5 includes a summary along with suggestions for future research.

2. Methodology

In this study, we use the Regional Atmospheric Modeling System (RAMS; Pielke et al. 1992; Walko et al. 1995), version 3b, configured as in MC02, but with modifications and improvements (see the appendix). The model is nonhydrostatic and solves the compressible equations of motion (Tripoli and Cotton 1982) using a time-splitting technique (Klemp and Wilhelmson 1978). In addition to solving for the three Cartesian velocities, ice-liquid water potential temperature (Tripoli and Cotton 1981), and pressure, it also prognoses six hydrometeor species (rain, hail, graupel, pristine ice, snow, and aggregates) and employs a diagnostic equation to obtain temperature and the mixing ratios of water vapor and cloud water. Particle number concentration is additionally prognosed for pristine ice. Subgrid mixing processes are parameterized using the deformation-based scheme of Smagorinsky (1963), with the stability modifications of Lilly (1962). Boundary layer momentum fluxes are included, but surface fluxes

of heat and moisture are not used here. Microphysical parameter values, used to determine the size distributions of the various particle species, are held fixed in the present research to simplify interpretation of the simulation results. Sensitivities of the simulations to variations in some of the basic microphysical parameters will be reported in a future paper. Bryan and Fritsch (2004) have shown that the RAMS formulation of ice-liquid potential temperature contains a cold bias, but this bias is likely not large enough to have a major impact on the broad trends seen in these simulations.

As in MW01 and MC02, we construct our idealized starting environmental profiles using the analytical function described in the appendix of MW01. This function consists of the scaled product of linearly increasing and exponentially decreasing functions of altitude relative to a prespecified LFC. Thus, our parcel buoyancy profile $b(z')$ is given by

$$b(z') = E\frac{m^2}{H^2}z' \exp\left(-\frac{m}{H}z'\right), \tag{1}$$

where z' is altitude above the prescribed LFC, E is a prescribed CAPE, H is a vertical scale having the value 14.5 km, and m is a profile shape compression parameter. The buoyancies thus defined are taken relative to a pseudoadiabat having constant θ_e as defined by Bolton (1980). Our environmental temperature profiles are obtained by subtracting the temperature differences implied by the prescribed buoyancy profiles from the temperatures of the pseudoadiabat.

As mentioned earlier, the present simulation results are part of an expanded parameter space study derived from MW01 and MC02. In this eight-dimensional parameter space study, we have performed experiments covering a wider range of conditions than those examined in MW01 and MC02. The expanded range of conditions involves not only new environmental parameters, but also consideration of additional values of those basic parameters used in MW01 and MC02. For example, as in MW01 and MC02, we still consider SBCAPE-P values $E = 800$ and 2000 J kg^{-1}, but now also consider a third value $E = 3200$ J kg^{-1}. For hodograph radius, we still consider 12 m s^{-1}, but also now examine 8 and 16 m s^{-1} radii. Profile shape parameter values for both buoyancy (m) and vertical shear (n) distributions are slightly different from those used in MW01 and MC02, and are listed in Table 1. We still specify mixed-layer and moist layer depths to extend from the surface to just above either model level 2 or 6, with the option for some experiments to have a moist layer deeper than the mixed layer, as described in MC02. Note that our "mixed" or "subcloud" layer is not truly well mixed, but instead simply has a fixed static stability and lapse rate, but with constant θ_e, such that the low-level thermodynamic structures of our environments satisfy the critical constraint that they do not mix out during our 2-h simulation time period. Thus, each level within our subcloud layer features its own LCL altitude, but for convenience we will refer to an experiment's LCL as being that associated with the model level at the top of the mixed layer. The LFC heights for our experiments do, however, correspond straightforwardly to the altitudes of the tops of our moist (i.e., constant θ_e) layers. For more details, please see item 3 in the appendix.

In this paper, we focus on the addition of a new environmental parameter, the LCL temperature, which is a good proxy for the environmental PW. Because the LCL temperature serves as the anchor for our full profile of designed environmental temperature, cases with low LCL temperatures feature colder temperatures aloft and smaller amounts of PW. Our LCL temperatures are specified in two regimes: one is identical to the very warm and moist tropical air mass regime already reported in MW01 and MC02, while the other is cooler and drier, with roughly half the PW of our previously published data. Note that it is possible to create starting environmental soundings having different PW values but similar temperature profiles. However, this requires changes in the free-tropospheric environmental relative humidity, which is controlled by another of our eight key parameters, and is the subject of a separate investigation. All simulations discussed in MW01, MC02, and this paper feature free-tropospheric relative humidity profiles that are specified to be a constant 90%, with respect to either water or ice, as the environmental temperature dictates.

As before, our low-LCL, high-PW cases (PW = 60 mm), feature values of pressure, temperature, and dewpoint at model level 2 (near $z = 0.5$ km above the surface) of 965 hPa, 23.5°C, and 23.0°C, respectively. To construct environmental temperature and moisture profiles for the new low-PW (PW = 30 mm) cases, we simply reduce the low-LCL-case temperatures and dewpoints by 8.0°C. To simulate high-LCL cases with high PW, we use the approach of MC02, and specify a pressure, temperature, and dewpoint at model level 6 (near $z = 1.6$ km above the surface) of 844 hPa, 18.8°C, and 18.3°C, respectively. For the high-LCL, low-PW cases, the temperatures and dewpoints are reduced by 8.74°C, to ensure that undilute updraft θ_e values are the same as for the low-LCL, low-PW cases. With these conditions, the updraft θ_e values for our high-PW cases are 354.3 K, and, for our low-PW cases, 323.4 K. We further specify isothermal stratospheric conditions with temperatures of −68°C for the high-PW cases, and

TABLE 1. Experiment nomenclatures.

Pseudoadiabatic CAPE parameter e
- 1 = 800 J kg^{-1}
- 2 = 2000 J kg^{-1}
- 3 = 3200 J kg^{-1}

Hodograph radius parameter c (or s)
- c = curved
- s = straight
- 1 = 8 m s^{-1}
- 2 = 12 m s^{-1}
- 3 = 16 m s^{-1}

Buoyancy shape parameter m
- 1 = 1.56 implies Z'_b = 9.3 km
- 2 = 1.88 implies Z'_b = 7.7 km
- 3 = 2.38 implies Z'_b = 6.1 km
- 4 = 3.22 implies Z'_b = 4.5 km
- 5 = 5.00 implies Z'_b = 2.9 km

(where Z'_b is the altitude of maximum buoyancy, relative to the LFC)

Wind profile shape parameter n
- 1 = 1.56 implies Z'_v = 9.3 km
- 2 = 1.88 implies Z'_v = 7.7 km
- 3 = 2.38 implies Z'_v = 6.1 km
- 4 = 3.22 implies Z'_v = 4.5 km
- 5 = 5.00 implies Z'_v = 2.9 km

(where Z'_v is the altitude of max v wind, relative to the LCL, in an assumed curved hodograph situation; for straight hodographs, a curved hodograph is first constructed, then unfolded into a straight line, ensuring that the shear profiles are identical for both curved and straight hodographs with similar specifications; note that the successive choices of m and n are designed to yield a series of altitudes of max parcel buoyancy and v wind that differ by roughly the same amount, about 1.6 km)

LCL height (actually mixed-layer depth) index k
- 2 = 0.5 km
- 6 = 1.6 km

LFC height (actually moist layer depth) index f
- 2 = 0.5 km
- 6 = 1.6 km

PW (implemented as LCL temperature T_L) parameter p
- 3 = 30 mm (implies T_L = 15.5°C for k = 2)
- 6 = 60 mm (implies T_L = 23.5°C for k = 2)

Free-tropospheric relative humidity parameter h
- 6 = 60% everywhere in the troposphere above the LFC
- 7 = 70% everywhere in the troposphere above the LFC
- 8 = 80% everywhere in the troposphere above the LFC
- 9 = 90% everywhere in the troposphere above the LFC

−94°C for the low-PW cases; these specifications yield equilibrium levels near 14.4 km, or just above the tropopause, for all simulations.

A listing of all allowable values of the eight environmental parameters used by us in our full parameter space study is given in Table 1. Note that the reduced mean and narrower range of specified values for m and n implies an upward shift and expansion of the range of values of the altitudes of maximum buoyancy and maximum v wind in our starting soundings, as compared to those used in the earlier studies MW01 and MC02. Our current selection of values of m and n are still, however, designed to provide a set of altitudes of maximum buoyancy and v wind that step by approximately constant 1.6-km amounts in the vertical.

For a parameter space study embracing eight environmental variables, it was necessary to devise an experiment nomenclature that would concisely define the vector of parameter values used in each experiment, while still retaining some mnemonic character. Our solution was to assign experiment names using an alphanumeric string of eight pairs of characters and numbers,

with each character representing the name of one of the environmental parameters, and the number paired with it representing an integer code for the actual value assigned. The characters and their allowable coded integer values are listed in Table 1. As can be seen from the table, a sample experiment name "*e2c2m4n4k2f6p3h9*" is readily decoded as featuring SBCAPE-P of 2000 J kg^{-1}; a curved hodograph with radius of 12 m s^{-1}; buoyancy and shear profile compression parameters of 3.22 (implying an altitude of maximum buoyancy and v wind of 4.5 km above the LFC and LCL, respectively); a mixed-layer depth (LCL height) encompassing the first two model layers, or about 0.5 km above the surface; a moist layer depth (LFC height) spanning the first six model layers, or about 1.6 km above the surface; an environmental PW of about 30 mm (actually specified as an LCL temperature of 23.5°C); and a free-tropospheric relative humidity of 90%. While this nomenclature may seem cumbersome at first, it is actually easy to master, and allows for straightforward and precise description of each experiment, or even sets of experiments, with a minimum of potential for confusion. For example, the main thrust of the present paper is an examination of the behavior of the "*p3*" (i.e., low PW, or cool environment) versus "*p6*" (i.e., high PW, or warm environment) storms. In previous papers leading up to the present parameter space study, MW01 dealt primarily with the impacts of variations of the profile shape parameters *m* and *n*, while MC02 dealt primarily with the impacts of variations in mixed-layer depth parameter *k* and moist layer depth parameter *f*.

For our simulation experiments, we use a mesh with 500-m horizontal spacing and total extent of 75 km in both horizontal directions. Although Bryan et al. (2003) argue that even finer grid resolution is desirable for convective storm simulations, use of a finer grid would have greatly increased the length of the simulations and the volume of computations and storage, and would have made this project infeasible. We are encouraged, however, that our 500-m mesh at least begins to fall within the regimes tested by Bryan et al. (2003) that resolve the peak in the turbulence kinetic energy spectrum, which, for example, 1000-m meshes fail to do.

In all our simulations, lateral boundaries are open, and in the vertical, we use a stretched mesh having spacing of 250 m at the bottom and 750 m at 20-km altitude. Our upper boundary, which lies at 24.5 km, is specified to be a rigid lid, but the uppermost 4.5 km of the domain is a Rayleigh friction layer that absorbs wave motions. In all simulations, we use a large time step of 4.0 s, with five acoustic time steps between. All simulations are executed for 120 min, with three-dimensional model output files saved every 5 min for postanalysis.

Initial conditions for all our simulations are horizontally homogeneous, with the exception of a convection-inducing circularly symmetric cosine-squared bubble placed near the center of the domain. As in MC02, all bubbles were centered vertically at $z = 0$, and had horizontal radii of 12 km and vertical radii of 2.5 km. The amplitudes of the bubbles were specified to be 2.5 K (3.0 K) for all *e1p6* (*e1p3*) experiments, 2.0 K (2.5 K) for all *e2p6* (*e2p3*) experiments, and 1.5 K (2.0 K) for all *e3p6* (*e3p3*) experiments. Slightly larger thermal perturbation amplitudes were used for the *p3* experiments compared to the *p6* experiments in order to ensure that the θ_e perturbations associated with the bubbles, which are important indicators of the strength of the initial bubble forcing, were more comparable across pairs of *p3* and *p6* experiments. The variations in thermal bubble amplitude across varying *e* values correspond to amplitudes that are near or just above the smallest needed to produce a consistent and representative deep convective response across all experiments having that value of *e*, but the bubbles may not be perfectly optimized for some experiments, owing to our limited resources. In general, we attempted to use as small an assortment of bubble amplitudes as possible, consistent with promoting as many straightforward experiment intercomparisons as possible, while launching convection with adequate, but not excessive, thermal forcing. We believe our initiation specifications have produced simulations that capture correctly the trends within the sampled parameter space, and that our conclusions would not likely change significantly even if far more effort were expended to achieve perfect optimization of the warm bubbles for all the simulations.

Our strategy in this paper is to focus on results from a representative pair of experiments, denoted *e2c2m4n4k6f6p3h9* and *e2c2m4n4k6f6p6h9*, which have identical environmental specifications except for the *p*-parameter value. This approach ensures that any differences that emerge from the comparisons will be due only to variations in the value of the *p* parameter. Such comparisons are very difficult to perform in observational studies of storms, because of the near impossibility of finding pairs of cases where all key environmental parameters are identical except for one.

For completeness, we also present several scatterplot figures that describe relevant patterns of storm behavior across a large subset of our full parameter space. However, owing to the large volume of experiments in our full parameter space study, we restrict discussion in this paper to a tractable subset. In the scatterplot figures in this paper, we focus only on the 12 m s^{-1}

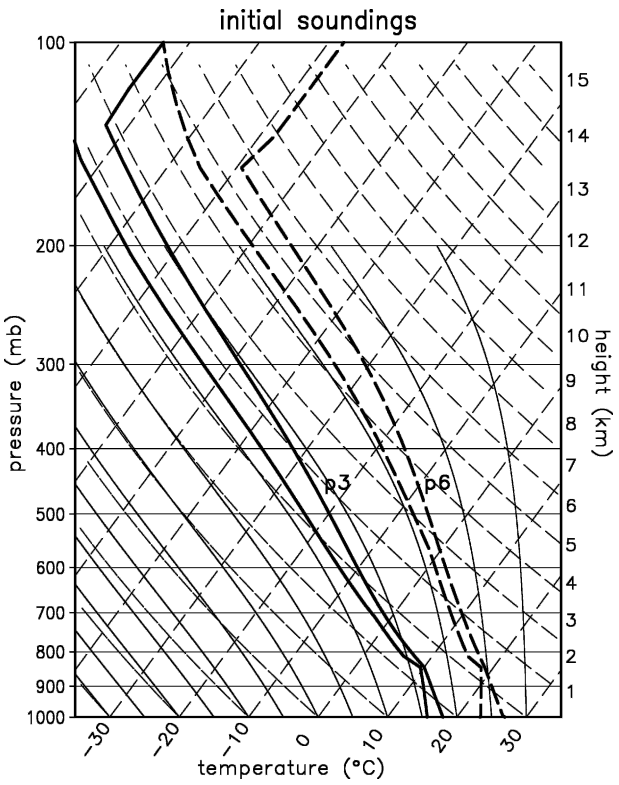

FIG. 1. Shapes of the temperature and moisture profiles used in the *e2c2m4n4k6f6p3h9* (low PW; solid) and *e2c2m4n4k6f6p6h9* (high PW; dashed) simulations, depicted in sounding form on skew *T*–log*p* charts. The altitudes shown along the right edge are valid only for the low-PW profile, with similar altitudes occurring at somewhat larger pressures in the warmer high-PW profile. The free-tropospheric relative humidity is always 90% relative to either water or ice, as ambient temperatures dictate, for the experiments.

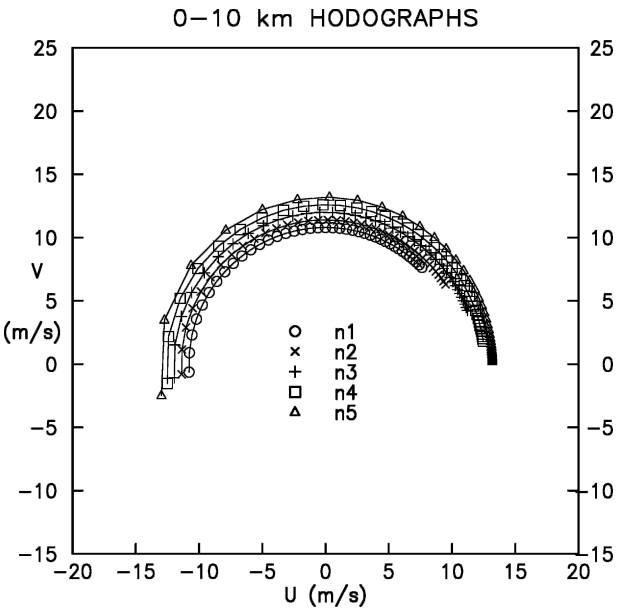

FIG. 2. Hodographs of the environmental wind profiles for the 0–10-km layer, for the five values of wind profile shape parameter *n* used in these experiments (see legend on plot). Each hodograph is marked with a distinctive symbol every 250 m of altitude. Each of five curves has actual hodograph radius of 12 m s^{-1}, but $n = 1$, $n = 2$, $n = 4$, and $n = 5$ are displaced slightly to show the distribution of 250-m data points clearly.

hodograph radius (i.e., "*c2*") experiments, because of the frequency of occurrence of their shear values in the severe weather climatology, and the apparent representativeness of the patterns and trends seen in their results.

3. Results

We now present detailed results from our selected pair of experiments, *e2c2m4n4k6f6p3h9* and *e2c2m4n4k6f6p6h9*. They are associated with SBCAPE-P values of 2000 J kg^{-1}, a hodograph radius of 12 m s^{-1}, concentrated buoyancy and shear profile shapes, deep mixed and moist layers, and free-tropospheric relative humidity of 90%. As it happens, these simulations show trends in behavior across variations in PW that are seen in nearly every other matched simulation pair in our large parameter space.

The thermodynamic profiles and hodographs used in these two simulations are illustrated in Figs. 1 and 2, respectively. In the skew *T*–log*p* diagrams of Fig. 1, hydrostatic considerations cause the high-PW *p6* environment profile to meet the tropopause at a higher pressure than its *p3* counterpart, but in both cases the tropopause occurs at the same geometric altitude, 14 km. The *n4* hodograph curve shown in Fig. 2 applies to both experiments discussed in detail here.

a. Overview and maps of two simulations

In Figs. 3 and 4 we present maps of storm structure at selected times for the *p3* and *p6* experiments, respectively. Times shown are 30, 60, 90, and 120 min into the simulations, and are chosen to provide only a rough overview of the evolution of the simulated storms. As in MW01 and MC02, the maps depict contoured updraft speeds at an altitude of 1.9 km above the LFC, shaded contours of near-surface ($z = 127$ m) rainwater mixing ratio, and near-surface wind vectors. Unlike the maps in MW01 and MC02, however, the maps herein feature ground-relative winds, with vector head size coded to differentiate between rain-cooled outflow (narrow heads) and undisturbed warm inflow (wide heads).

In selecting the storm of interest to highlight in these

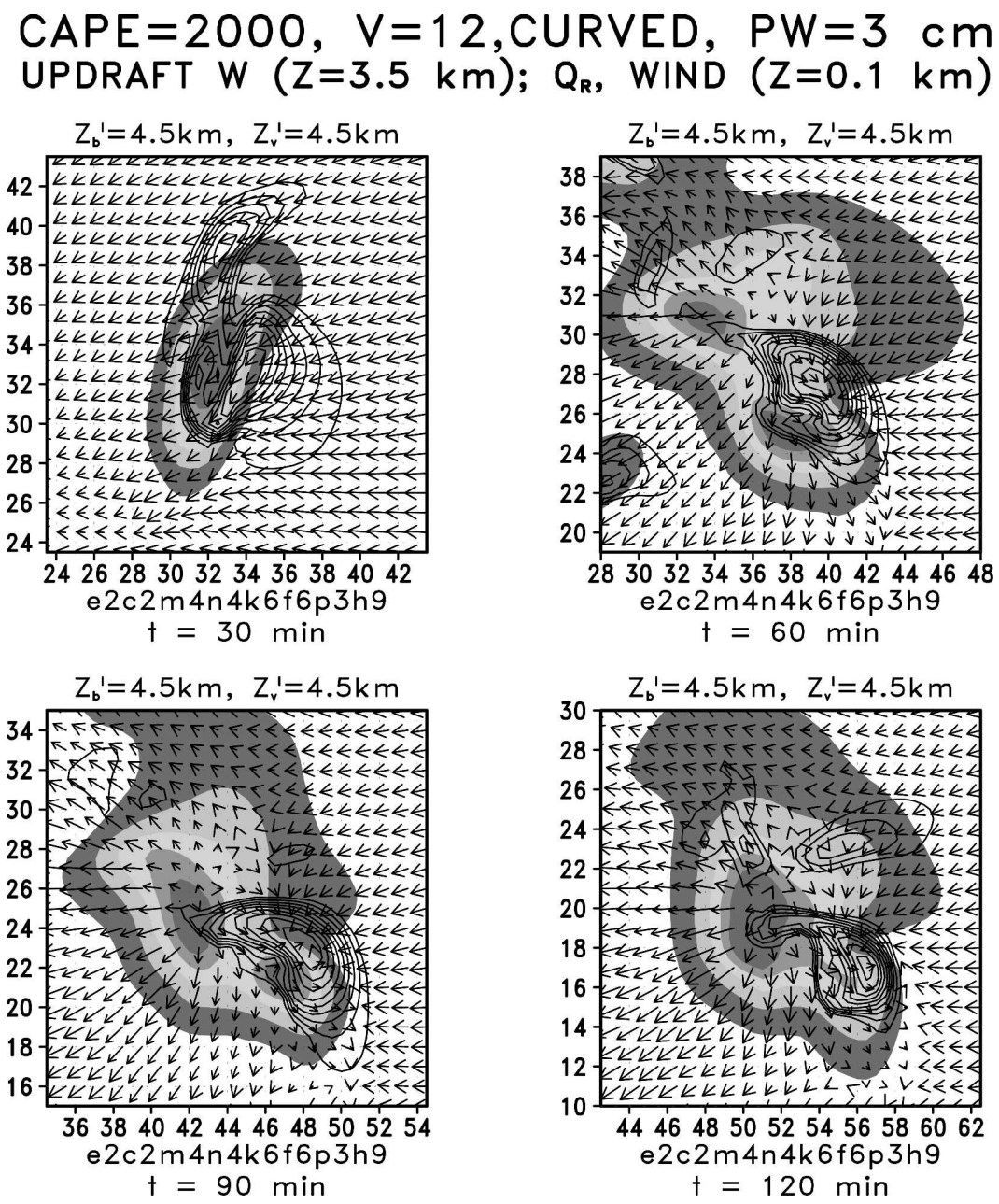

FIG. 3. Maps of evolving simulated updraft velocity w at $z = 3.5$ km (contoured at 2 m s^{-1} intervals), rainwater mixing ratio q_r at $z = 0.127$ km (shaded starting at 0.25, 1.0, 2.0, 3.0, and 4.0 g kg^{-1} values), and horizontal ground-relative wind vectors (every other vector removed) at $z = 0.127$ km for the low-PW *e2c2m4n4k6f6p3h9* simulation. Full experiment names and times (min) are listed beneath each map for reference. Coordinates relative to the full simulation domain are marked at 2-km intervals along the sides of the plots. Vectors are scaled such that a length of 1 km on the plots corresponds to a wind speed of 12.5 m s^{-1}. Heads of wind vectors are wide for undisturbed warm inflow, but narrow for rain-cooled outflow air.

maps, emphasis was placed on right-moving storms that attained the largest size and greatest intensity during the second hour of the simulations. Additional aspects of the temporal variability of these and our other storms can be gauged by examining the scatterplots to be presented later.

In Figs. 3–4, both storms can be seen to display supercell characteristics, based on early updraft splitting, mature updraft configuration and location relative to the precipitation shield, and also updraft rotation (not shown). However, several significant differences in the storm precipitation and flow structure fields are also

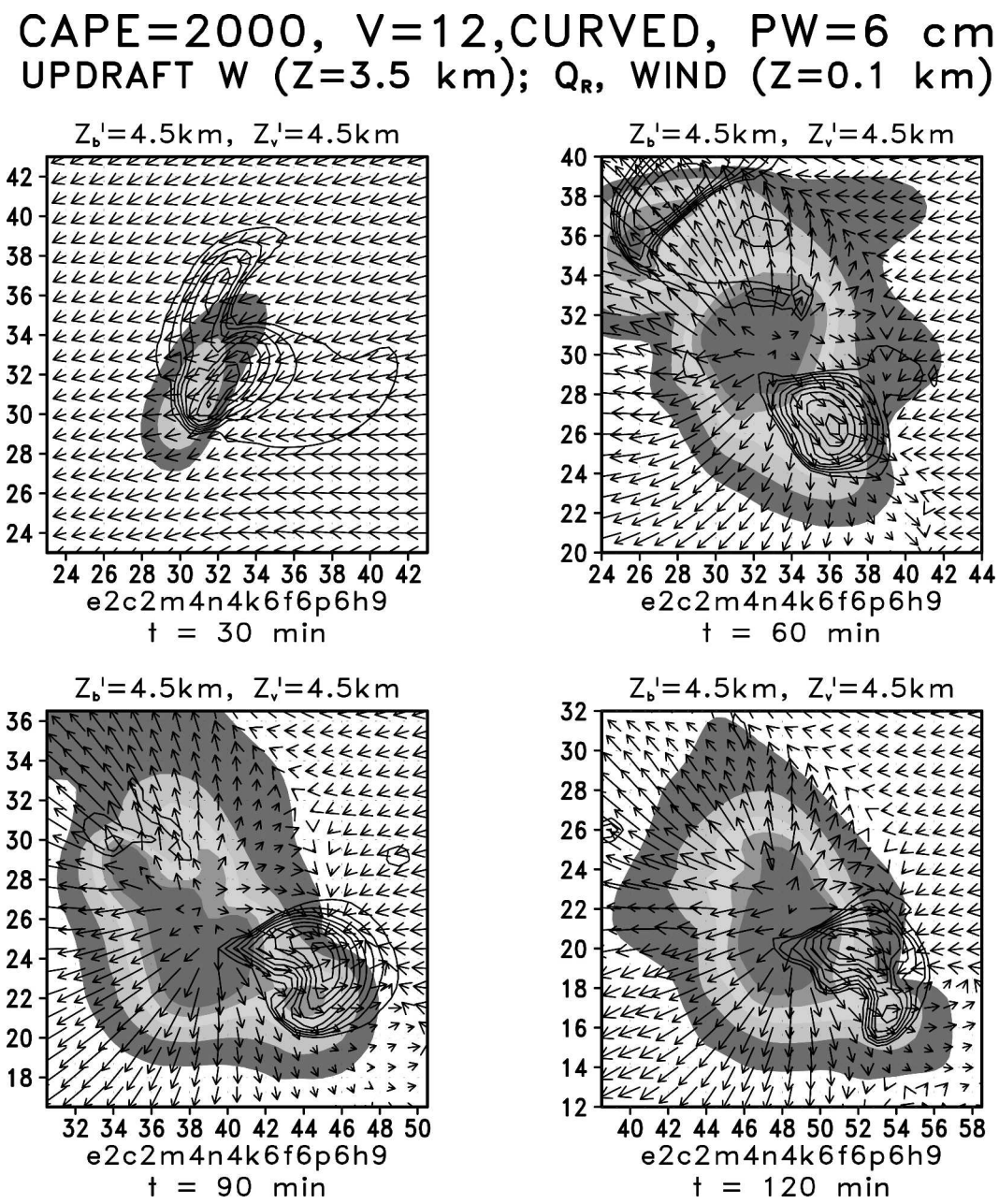

FIG. 4. Same as in Fig. 3, but for the high-PW *e2c2m4n4k6f6p6h9* simulation.

evident. The high-PW *p6* storm (Fig. 4) shows a consistent tendency to have a larger core of intense surface precipitation than the low-PW *p3* storm (Fig. 3), although the total precipitation footprints, including very light rain, do not differ appreciably in size. The core of the low-PW storm also contains more hail than the high-PW storm (not shown). Inspection of the direction of the wind vectors also reveals that the high-PW storm produces a larger field of surface outflow, with outflow often reaching to the edge of the light rain area on the eastern (inflow) flank, and beyond the edge on the western (outflow) flank. In the low-PW storm, undisturbed inflow frequently penetrates deeper into the precipitation footprint area. The outflow flank (western side) of the high-PW storm also exhibits more widespread cool outflow, based on the proportion of wind vectors drawn with small heads. This suggests that the outflow of the high-PW storm is colder relative to its environment than that of the low-PW storm, a supposition that is borne out by examination of the tempera-

tures in the surface outflow (not shown). Finally, Fig. 5 shows that the peak updraft speeds in the high-PW storm during the second hour, 47 m s^{-1}, are distinctly weaker than those in the low-PW storm, 59 m s^{-1}. Figure 5 also shows that the high-PW storm generates low-level downdrafts that reach 27 m s^{-1}, whereas the low-PW storm downdrafts never exceed 14 m s^{-1}. The latter finding is consistent with the surface outflow patterns described above.

b. *Scatterplots of e1c2h9, e2c2h9, and e3c2h9 simulations*

We now consider how the scatterplots of all second-hour 5-min values of three key storm intensity parameters look when partitioned against environmental PW. In presenting these scatterplots, we will also take advantage of the compactness of the graphics to present results from the *e1* and *e3* portions of the *c2* part of the parameter space, as well as from other parts of *e2*. In doing so, we will be able to demonstrate the representativeness of the results obtained from the two cases studied in detail here.

Figure 6 shows the second-hour peak updraft velocity values $w_{\max}$ from the most significant storms in the *e1c2h9* (Fig. 6a), *e2c2h9* (Fig. 6b), and *e3c2h9* (Fig. 6c) experiment series, as a function of environmental PW. Because each experiment has a fixed value of PW, any variability of w_{max} during the second hour causes the data points for that experiment to become distributed along a vertical "stripe." Note that the *p3* experiments tend to cluster in a series of stripes near PW = 30 mm, with the *p6* experiments near PW = 60 mm. Within each of these clusters, there are six vertical sets of paired experiments depicted, representing the two choices of *m* distributed across the three *k2f2*, *k2f6,* and *k6f6* LCL-LFC parameter subsets. Some of these vertical stripes of data overlie other stripes, because their values of PW are almost indistinguishable. In general, the stripes of data within each cluster show small increases in PW from the *k2f2* through *k6f6* to *k2f6* experiment series.

The scatterplots of $w_{\max}$ versus PW tend to confirm the impressions from the data in Figs. 3–5. The peak values of $w_{\max}$ are nearly always larger in the *p3* clusters than they are in the *p6*, although, of course, there is some overlap evident. Nevertheless, if one defines storm overturning efficiency (see, e.g., MW01 and MC02) in terms of the largest peak updraft velocity attained by a storm during its mature phase, relative to the maximum updraft speed predicted by pseudoadiabatic parcel theory, then it is clear that the *p3* storms usually achieve greater overturning efficiency than the *p6* storms, all other environmental key parameters being equal. This general pattern is true for all CAPE values considered here.

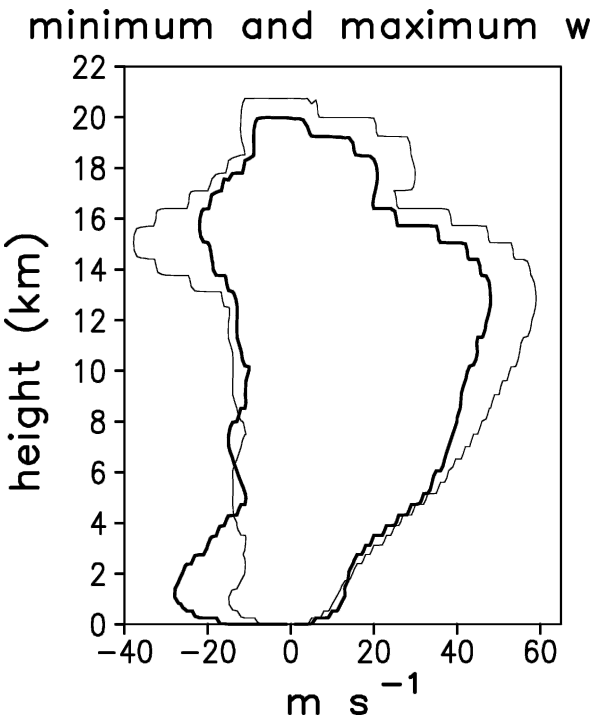

FIG. 5. Envelope of peak vertical velocities as a function of altitude for the second hour of the low-PW *e2c2m4n4k6f6p3h9* simulation (light line) and the high-PW *e2c2m4n4k6f6p6h9* simulation (bold line).

Figure 7 depicts peak surface precipitation rates for the same storms as shown in Fig. 6. Here the trends are somewhat different from those seen in Fig. 6. Maximum surface precipitation rates are largest within the *p6* clusters, the opposite of what is seen for w_{max}. There is one exception involving the *e1* storms, where enhancement of storm updrafts is sufficient to cause larger surface precipitation rates in a few *p3* cases. However, the differences between the precipitation rates are always small. Interestingly, the *p6* clusters of experiments also include storms that exhibit the weakest surface precipitation rates. It thus appears that the *p6* storm environments support a somewhat wider range of precipitation rates than the *p3* environments.

Precipitation efficiency may be defined as the ratio of rainfall at the ground to condensation (Ferrier et al. 1996), to water vapor inflow (Doswell et al. 1996; Fankhauser 1988), or to precipitable water (Market et al. 2003). With the first two definitions, we are measuring the conversion of cloud water to precipitating hydrometeors by microphysical processes, while the third definition is a climatologically or environmentally based measure of the production of precipitation. We

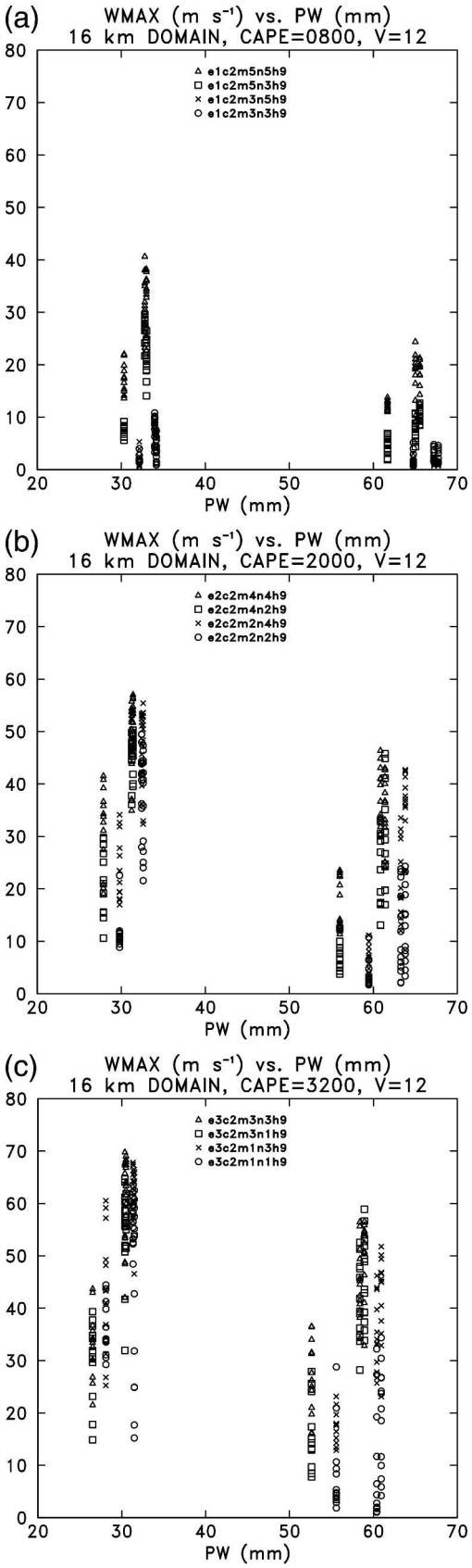

therefore refer to the first two definitions as microphysical precipitation efficiency (MPE) and the third as environmental or climatological precipitation efficiency (CPE).

Scatterplots of the CPE versus PW for all the storms shown in Figs. 6–7 are given in Fig. 8. This figure clearly shows the enhancement of CPE associated with the *p3* storms, with the low-PW storms frequently exhibiting CPE values almost twice those of the *p6* storms. Recall that the actual PW of the *p6* storms is roughly twice that of their *p3* counterparts.

4. Discussion

a. Updrafts and storm precipitation efficiency

The finding of larger CPE values in the colder *p3* storms (Fig. 8) merits further exploration. We find the updrafts in all storms are saturated with respect to water up to about −20°C. The cloud-base pressures are the same for all warm (*p6*) and cold (*p3*) environment experiment pairs, so that the distance between cloud base and −20°C is larger for the warmer (*p6*) soundings. If we estimate the amount of liquid condensate in a rising parcel by subtracting the q_v in the updrafts at −20°C from the q_v in the updrafts at the cloud base, it is obvious that the clouds in the warmer (*p6*) soundings have the potential to produce more cloud water. However, the average mixing ratios q_c of cloud water in the updrafts (Fig. 9) are generally about the same for all pairs of cold (*p3*) and warm (*p6*) soundings, except that the q_c extends higher for the warmer soundings, reaching −40°C for both. Above −20°C, as q_c begins to evaporate within the updraft, it also decreases with height due to autoconversion, collection and freezing. For the colder (*p3*) soundings, there is relatively less autoconversion and collection and more homogeneous freezing of cloud water (Fig. 10). The pristine crystals produced by this latter process grow rapidly by deposition, especially for the *p3* storms, but are only slowly converted to precipitation, as shown in Fig. 11. In this

←

FIG. 6. Scatterplot of peak updraft velocity WMAX (m s^{-1}) in the mature principal right-moving storms vs environmental PW (mm), for each 5-min history save made during the second hour of the (a) *e1c2h9*, (b) *e2c2h9*, and (c) *e3c2h9* simulations. Data from 5-min history saves are shown instead of hourly averages in order to provide a sense of the temporal variability of the data. All peak updrafts were evaluated within a 16-km subdomain centered on the main storm of interest. Distinct symbols (see legend on plot) are used for the various buoyancy and shear profile shapes associated with the *m2n2*, *m2n4*, *m4n2*, and *m4n4* experiment subsets.

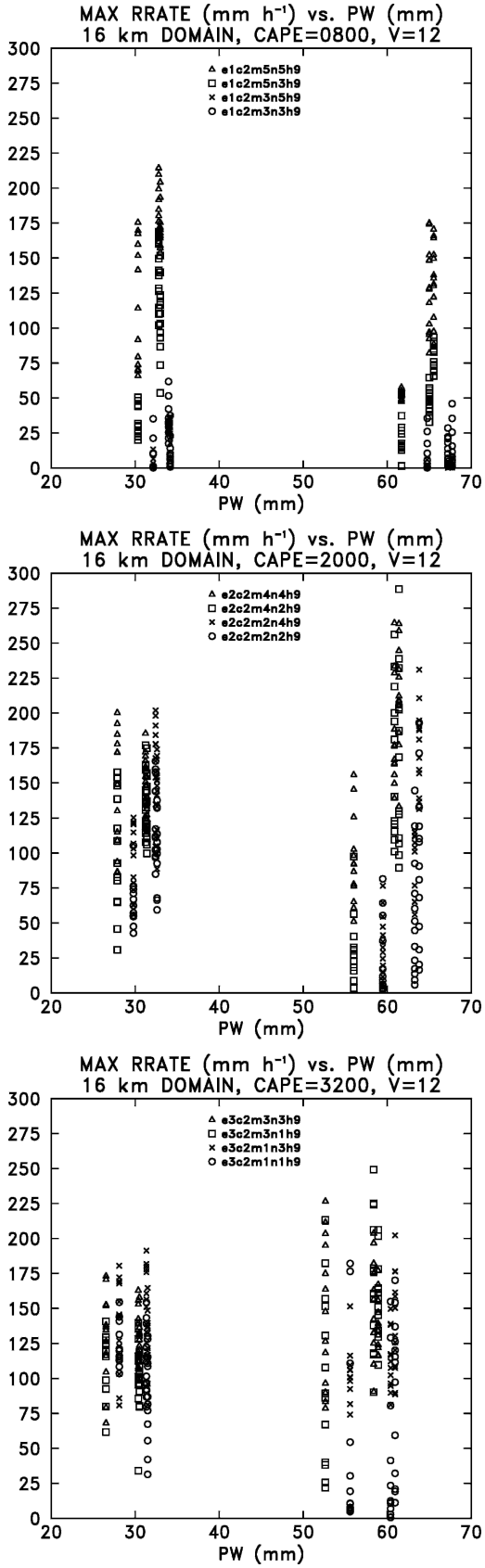

FIG. 7. Same as in Fig. 6, but for peak surface precipitation rate RRATE vs environmental PW for (a) *e1c2h9*, (b) *e2c2h9*, and (c) *e3c2h9* simulations.

latter figure, we compute the rate of production of precipitation by adding the rates of collection of pristine crystals by precipitating hydrometeors, aggregation of pristine crystals, and transfer from pristine crystals to snow, as described by Eq. (69) of Walko et al. (1995). With the colder *p3* soundings, therefore, storms tend to produce relatively less precipitation and generate larger or thicker cirrus anvils, a trend that is evident in Fig. 12, but is even more obvious in other experiment pairs (not shown). While this pattern holds true for all combinations of LCL and LFC height, it is particularly prominent when LFCs are high (*k2f6* or *k6f6* cases). However, because the *p3* updrafts tend to be stronger, they can produce almost the same precipitation rates at the ground as the warmer (*p6*) environment storms, despite less precipitable water (implying a larger CPE) and a relatively inefficient conversion of cloud water to precipitation (smaller MPE).

We must be careful to note that the autoconversion and collection and the homogeneous freezing of cloud water shown in Fig. 10 are averaged over the whole domain for the second hour of the simulations. Therefore, part of the explanation for the different magnitudes of the microphysical processes for clouds generated with cold (*p3*) and warm (*p6*) soundings lies in the shapes of the updraft mass flux profiles (Fig. 13). Averaged over space and time, the updraft mass flux tends to increase with height more rapidly with the colder (*p3*) soundings, suggesting that the condensation is occurring, on average, at a greater height, giving the cloud water q_c less chance to be collected before it freezes. This effect is in addition to the presence of shorter distances between cloud base and the freezing level in the *p3* environments. The smaller MPE with the colder soundings is therefore only a spatially and temporally integrated result, and would likely not be found following some individual parcels. To what extent is it directly associated with microphysical processes?

The smaller MPE in the colder (*p3*) soundings is in fact partly the result of cloud dynamics. With the colder soundings, the maximum updraft velocity increases more rapidly with height in the midtroposphere. Market et al. (2003) suggested that very large CAPE might lower the precipitation efficiency of storms because the presumed stronger updrafts of high-CAPE storms would eject more condensate out through the anvil before precipitation processes could reach completion.

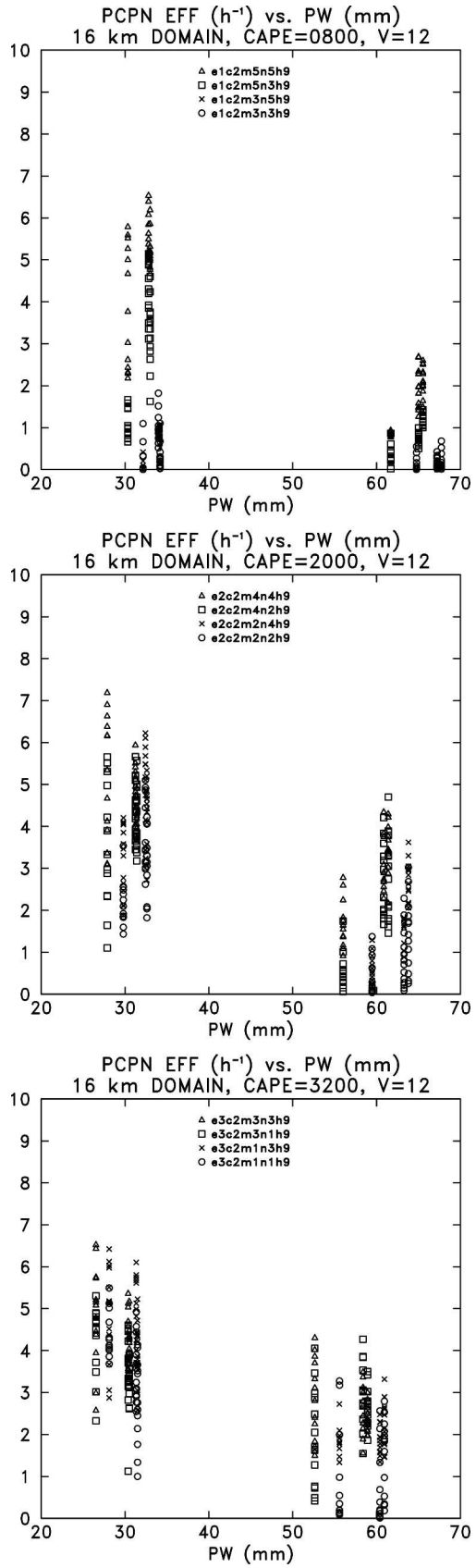

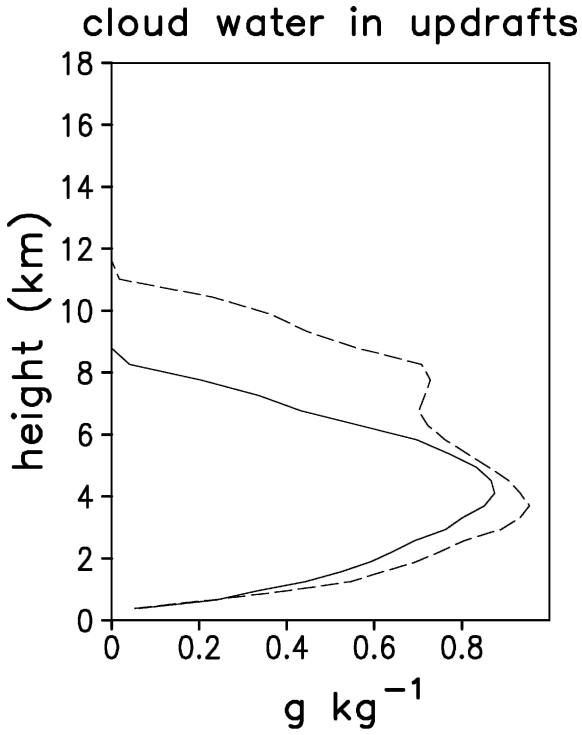

FIG. 9. Mean profiles of cloud water mixing ratio (g kg^{-1}) in updrafts for the low-PW *e2c2m4n4k6f6p3h9* (solid) and high-PW *e2c2m4n4k6f6p6h9* (dashed) experiments averaged over the whole domain for the second hour.

However, in the present simulations, microphysical processes are also directly relevant, the precipitation findings being not simply a result of the storm dynamics.

The rate of collection of cloud water by precipitating particles is proportional to the volume swept out by the precipitation per unit time [see Eq. (46) of Walko et al. 1995]. In the present simulations, as shown in Table 2, the diameters of the particles with the mean mass are set at 0.1, 0.3, and 0.1 cm for rain, hail, and graupel, respectively, and all three hydrometeors have gamma distributions with the same shape parameter $\nu = 1.5$. Very little cloud water is collected by snow or aggregates, and none by pristine crystals. The terminal velocities for rain, hail, and graupel are all proportional to the square roots of the respective particle diameters. Therefore, for the same mixing ratios, rain collects more cloud water than hail does, because the larger

←

FIG. 8. Same as in Figs. 6–7, but for peak surface CPE (i.e., peak surface precipitation rate divided by environmental PW) vs environmental PW for (a) *e1c2h9*, (b) *e2c2h9*, and (c) *e3c2h9* simulations.

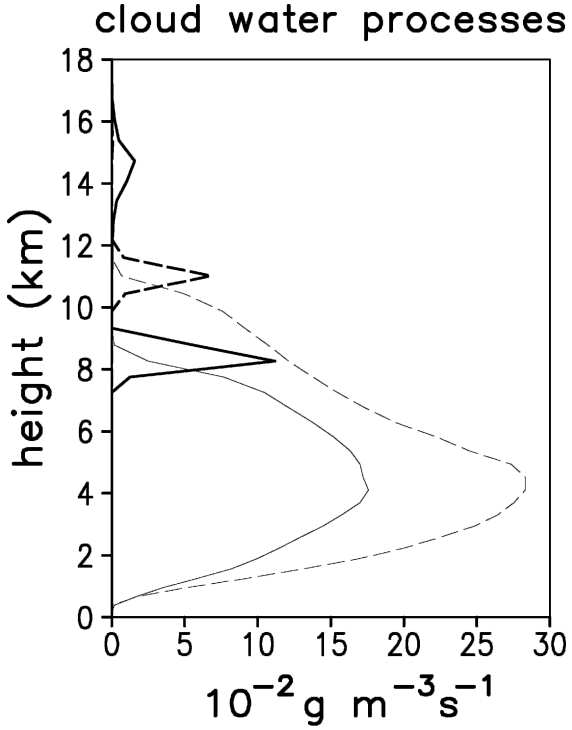

FIG. 10. Autoconversion plus collection of cloud water (thin lines) and homogeneous freezing (thick) of cloud water (10^{-2} g m^{-3} s^{-1}) for the low-PW *e2c2m4n4k6f6p3h9* (solid) and high-PW *e2c2m4n4k6f6p6h9* (dashed) experiments, averaged over the whole domain for the second hour.

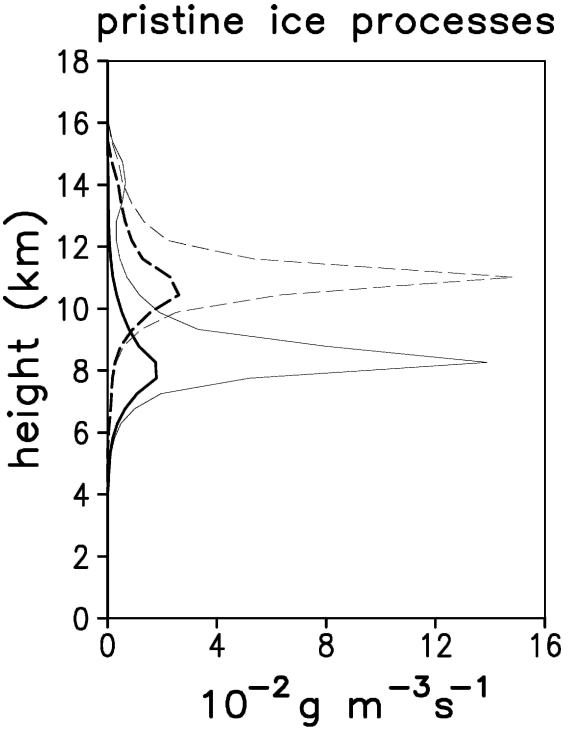

FIG. 11. Sum of collection and aggregation of pristine crystals and transfer of pristine crystals to snow (thick lines) and deposition onto pristine crystals (thin) (both in 10^{-2} g m^{-3} s^{-1} units) for the low-PW *e2c2m4n4k6f6p3h9* (solid) and high-PW *e2c2m4n4k6f6p6h9* (dashed) experiments, averaged over the whole domain for the second hour.

numbers of raindrops present more horizontal area to the cloud droplets, and the greater terminal velocities of hail cannot quite compensate for this. With the cooler *p3* (warmer *p6*) soundings, the updrafts have a shallower (deeper) layer warmer than 0°C, and consistent with this, have relatively less (more) rain compared to the amount of hail, as shown in Fig. 14. This explains why updrafts with the colder (warmer) soundings convert q_c to precipitation less (more) efficiently. The larger rate of collection of q_c with the warmer *p6* soundings is due mostly to collection by rain (see Fig. 15). Owing to their smaller density, graupel particles are much more numerous than raindrops or hailstones, for equal mixing ratios. Although graupel collects much more q_c than does an equal mixing ratio of rain, there is relatively little graupel in the stronger updrafts, and it is often found at higher altitudes than the hail, above the peak in the q_c mixing ratio (Fig. 14). These factors limit graupel's contribution to collection as compared to that by rain.

The point we are making here should not be confused with the results of several observational studies (Zipser and LeMone 1980; Willoughby et al. 1985) that have shown larger precipitation efficiency for maritime tropical convection compared to midlatitude continental convection. In those studies, a primary consideration was the weak vertical velocities for the maritime tropical clouds, a result perhaps as much related to differing buoyancy profile shapes and LFC heights as to environmental temperature and PW. Here, the difference between updraft velocities for warm (*p6*) and cold (*p3*) sounding pairs is not as large, especially in the lower troposphere, where the warm rain production occurs. This is because all other basic environmental parameters are the same across our *p3* and *p6* experiment pairs, unlike most observational studies.

Let us now consider the effects of freezing on updraft buoyancy in our two different temperature regimes. Suppose all freezing occurs at 0°C. If the liquid condensate mixing ratio is q_l, then the air temperature increase due to freezing of q_l is

$$\Delta T = q_l L_f / C_p, \tag{2}$$

where $L_f = 0.334(10)^6$ J kg^{-1} is the latent heat of fusion, and $C_p = 1005.7$ J kg^{-1} K^{-1} is the specific heat of air. We can estimate the buoyancy acceleration b as

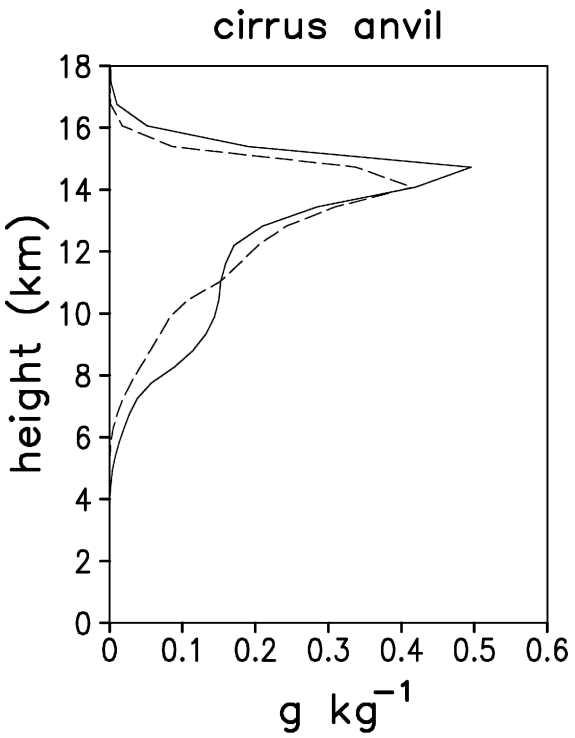

FIG. 12. Mixing ratio of pristine crystals + snow + aggregates (0.1 g kg^{-1}) for the low-PW *e2c2m4n4k6f6p3h9* (solid) and high-PW *e2c2m4n4k6f6p6h9* (dashed) experiments, averaged over the whole domain for the second hour.

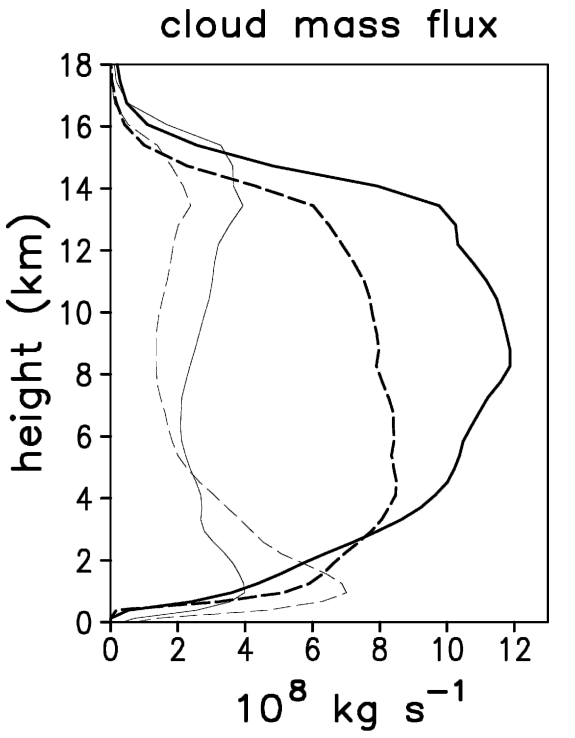

FIG. 13. Mean updraft (thick) and downdraft (thin) mass flux profiles (10^8 kg s^{-1}) for the low-PW *e2c2m4n4k6f6p3h9* (solid) and high-PW *e2c2m4n4k6f6p6h9* (dashed) experiments, averaged over the whole domain for the second hour.

$$b = g\left(\frac{T_p - T}{T} - q_l\right), \tag{3}$$

where T_p is the cloud updraft parcel temperature, T is the base-state temperature, and g is the acceleration due to gravity. Here we ignore the relatively small virtual temperature effects. The increase in buoyancy at 0°C due to freezing is then 1.22_{gq_l}, which is clearly 22% larger than the negative effect of the condensate loading on the buoyancy. It is true that if the freezing occurred at colder temperatures, the latent heat of fusion would be smaller, but this is compensated by the heat capacity of liquid water, which is about twice that of ice. If the freezing were to occur at a colder temperature, the liquid water would have supplied the additional heat (Kirchhoff's law; see Emanuel 1994, p. 115).

A larger condensate mixing ratio at the freezing level will therefore provide greater additional buoyancy to an updraft. Figure 16 shows the profiles of horizontally averaged updraft heating rates due to the release of latent heat of fusion, in units of kelvins per second, averaged over the second hour of each simulation, divided by the mean upward velocities. After multiplying by 1000, this is the fusion heating per kilometer of rise of an updraft parcel. The freezing processes simulated here include the freezing of rain near −10°C, the riming of cloud water between 0° and −40°C, and homogeneous freezing of any remaining cloud water at −40°C. The uppermost maxima in the profiles of Fig. 16 are due to both homogeneous freezing and deposition onto the resulting ice crystals. This is the source of the cirrus anvils, while the freezing at lower altitudes produces frozen precipitation.

Notice in Fig. 16 that the warmer (*p6*) sounding has a larger peak in the vertical profile of release of latent heat of fusion, indicating a larger mixing ratio of condensate rising through the freezing layer. Why then are the maximum upward velocities generally smaller for the warmer soundings?

The answer has to do primarily with events occurring at low levels in the updrafts of the storms. While there is a larger amount of freezing and its associated extra buoyancy generation in the warmer *p6* storms, almost all of the extra buoyancy occurs at high altitudes, and has only a minor impact on that storm's updraft strength. For the colder *p3* storms, however, at least some of the freezing effects begin at much lower altitudes. Figure 16 shows that the heating is positive and increases with height from 0°C up to about −8°C, at altitudes of roughly 3–4 km for the *p3* cases and 5–6 km

TABLE 2. Model numerical and physical parameters.

Parameter	Value
Horizontal resolution Δx, Δy	500 m
Mean vertical resolution Δz	500 m
Vertical resolution at $z = 0$, Δz_0	250 m
Vertical resolution at $z = 20$ km, Δz_{20}	750 m
Large time step Δt	4.0 s
Small time step Δt_s	0.8 s
Coriolis parameter	0.0 s^{-1}
Surface roughness length z_0	1.0 cm
Subgrid turbulence scheme IDIFFK	3 (isotropic)
Deformation-relative horizontal mixing coef min AKMIN	1.0
Horizontal mixing coef min	298 $m^2 s^{-1}$
Mixing length scale factor	0.30
Thermal bubble amplitude $\Delta\theta$	1.5–3.0 K
Thermal bubble horizontal radius	12.0 km
Thermal bubble vertical radius	2.5 km
Thermal bubble center altitude	0.0 km
No. of concentration of cloud droplets N_t	300 cm^{-3}
Diameter of mean-mass raindrops D_m	0.1 cm
Diameter of mean-mass snow crystals D_m	0.1 cm
Diameter of mean-mass aggregates D_m	0.1 cm
Diameter of mean-mass graupel D_m	0.1 cm
Diameter of mean-mass hailstones D_m	0.3 cm
Distribution shape parameter ν, cloud droplets	1.0
Distribution shape parameter ν, raindrops	1.5
Distribution shape parameter ν, pristine crystals	1.0
Distribution shape parameter ν, snow crystals	1.5
Distribution shape parameter ν, aggregates	1.5
Distribution shape parameter ν, graupel	1.5
Distribution shape parameter ν, hailstones	1.5

for the *p6* cases. As a result of the differing distributions of fusion heating in the *p3* versus *p6* cases, the layer between 4.3 and 6.1 km features θ_v' in updrafts that is generally more skewed toward large positive values in the colder (*p3*) soundings (Fig. 17). This means that larger buoyancy is acting at these levels in the updrafts, which in turn promotes enhanced buoyancy at higher altitudes, invigorating the updraft throughout much of its depth. This finding is somewhat similar to that obtained by McCaul and Weisman (1996, 2001), where storms were found to be stronger when the buoyancy in similar CAPE environments was concentrated at low levels, irrespective of the overall environmental temperature regime. One fundamental difference, however, is that in the MW01 study, the enhanced buoyancy at low levels occurred by design in certain experiments only, whereas here it occurs as a by-product of the differing microphysics in the cold (*p3*) environments compared to the warm (*p6*) environments, even when the prescribed buoyancy profile shapes, which ignored the effects of the latent heat of fusion, are specified to be the same.

Of comparable or even greater importance is the fact that the rate of production of condensate in the low levels of the warmer *p6* updrafts is greater than that in the colder *p3* updrafts. To some extent, this effect can be quantified by considering reversible CAPE theory, which assumes that all condensate remains in the updraft parcel. Although the reversible theory predicts that condensate loading increases monotonically with height up to the updraft summit, which is at variance with observations and these simulations, it nevertheless tends to reproduce the low-level profile of condensate loading with some fidelity. We have computed SBCAPE-RL for the *p3* and *p6* cases, and find values of 1630 and 1018 J kg^{-1}, respectively. These imply maximum updraft speeds of 57 and 45 m s^{-1}, which are smaller than those actually simulated (59 and 47 m s^{-1}; see Fig. 5). Although the peak updraft speeds predicted by SBCAPE-RL are only slightly smaller than those seen in the simulations, any deficit is significant, because mixing and pressure gradient accelerations are ignored, and these frequently act to restrain the peak updraft speeds in real and simulated storms. If we include the effects of fusion heating in our reversible CAPE theory, by assuming all freezing of hydrometeors occurs at −10°C (see Williams and Renno 1993), we then obtain SBCAPE-RLF values of 2397 and 2034 J kg^{-1}, respectively, for the *p3* and *p6* cases. These latter values imply peak updraft speeds of 69 and 64 m s^{-1}, which are larger than those seen in the simulations. Note that the pseudoadiabatic CAPE theory predicts maximum updraft speeds of 63 m s^{-1} for both warm and cold environments. Thus, the simulated storms described here contain updrafts whose peak velocities lie in between the extremes predicted by the various CAPE theories. Only the reversible theory, however, is able to predict that the *p6* updrafts are weaker than the *p3*.

Condensate loading effects are also capable of helping to explain why storm updrafts benefit when parcel buoyancy is concentrated into the lower troposphere, as shown by MW01. In observed and simulated deep convective storms, peak values of condensate loading tend to occur in the lower parts of the storms. When environmental lapse rates are strong at low levels, parcel buoyancies derived from the heat released during condensation can be large enough to counteract the inhibition produced by the loading, whereas if the low-level lapse rates are not so strong, updraft parcels may not acquire enough condensation buoyancy to overcome the loading.

b. Downdrafts and evaporation of rain

The strength of a storm's cold surface outflow depends on the mass flux and the virtual temperature of

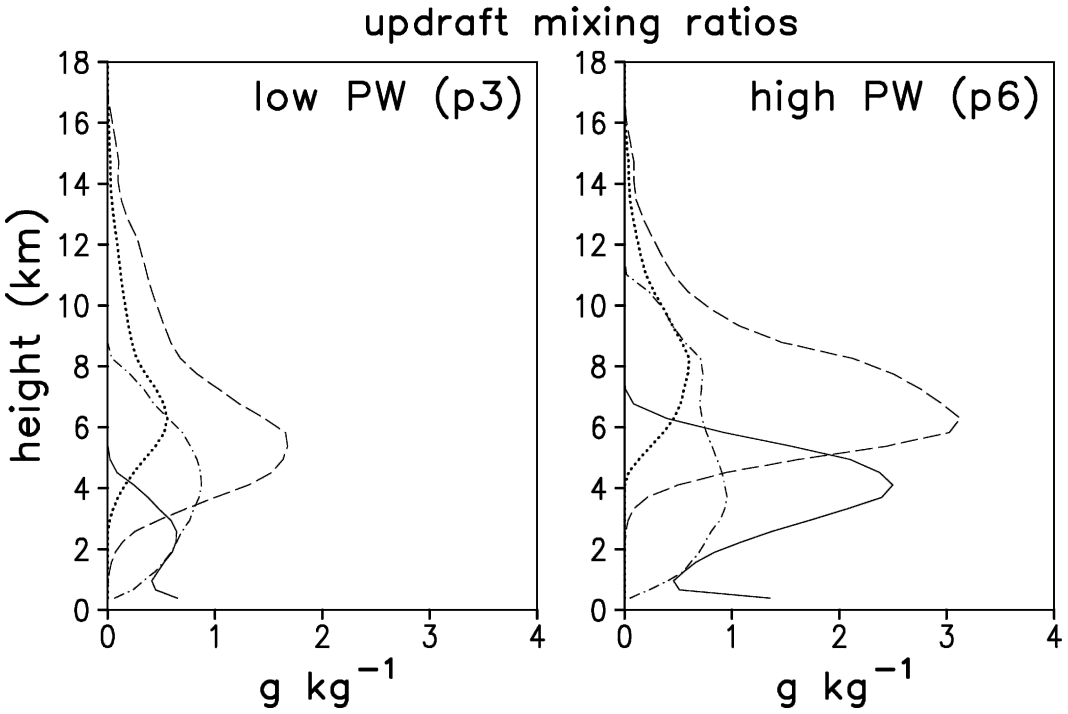

FIG. 14. Mean mixing ratios of rain (solid), cloud water (dot–dash), hail (dashed), and graupel (dots) (in g kg^{-1}) in updrafts for the low-PW *e2c2m4n4k6f6p3h9* (solid) and high-PW *e2c2m4n4k6f6p6h9* (dashed) experiments, averaged over the whole domain for the second hour.

the downdrafts that reach the surface, while outflow propagation speed also depends on the ambient wind shear. Our results indicate that clouds in the warmer (*p6*) environments generally have a larger ratio of downdraft to updraft mass flux in the lower troposphere (see Fig. 13). Recall (Fig. 5) that the peak downdraft in the *p3* storm reaches only 14 m s^{-1}, while in the *p6* storm it is almost twice as large, 27 m s^{-1}.

To determine whether the strength of the downdrafts depends directly on the properties of the environment, we repeated some of our experiments, but instead of using a warm bubble to initiate convection, we began with a circular column of condensate, having a mixing ratio of 5 g kg^{-1} at its center, decreasing outward to zero at a radius of 3 km. The condensate, which extends from the top of the PBL up to 10 km, is rain for $T \geq 0$°C, hail and graupel for $T \leq -10$°C, and a linearly varying mixture of the these species between those levels.

Averaged over time, for the pair of new simulations with warm (*p6*) and cold (*p3*) initial soundings, the virtual temperature deficits are similar and the cold outflows propagate at about the same speed (not shown). The downdraft mass fluxes (not shown) are not much different, but they are more often larger for the colder (*p3*) soundings. This demonstrates that the larger ratio of downdraft to updraft mass flux found in the warm (*p6*) experiments is largely due to the greater fallout of condensate from their updrafts, and not directly due to any properties of the initial sounding.

However, some characteristics of the downdrafts do depend directly on the environmental temperature profile. The rate of evaporation of rain or sublimation of ice in a downdraft is proportional to the difference between the saturation mixing ratio q_s at the temperature of the hydrometeor and the water vapor mixing ratio q_v in the downdraft. Ice therefore sublimates much more slowly than rain evaporates. Both of the simulations exhibit more evaporation than sublimation of precipitation (Fig. 18). The amplitudes of the sublimation profiles are roughly comparable for both the *p3* and *p6* cases, but evaporation is especially large for the latter case. The warmer *p6* sounding, having a deeper layer below the melting level, allows more of the falling precipitation to evaporate than does the colder sounding. In addition, although the rain that is evaporating is generally colder, relative to the surrounding air (Fig. 19b), in the warmer sounding than in the colder sounding, the excess mixing ratio at the surface of the raindrops is larger for the warmer sounding (Fig. 19a), because saturation vapor pressure increases exponentially with temperature. This also leads to more evaporation and reduced rainfall at the ground in the warmer sounding,

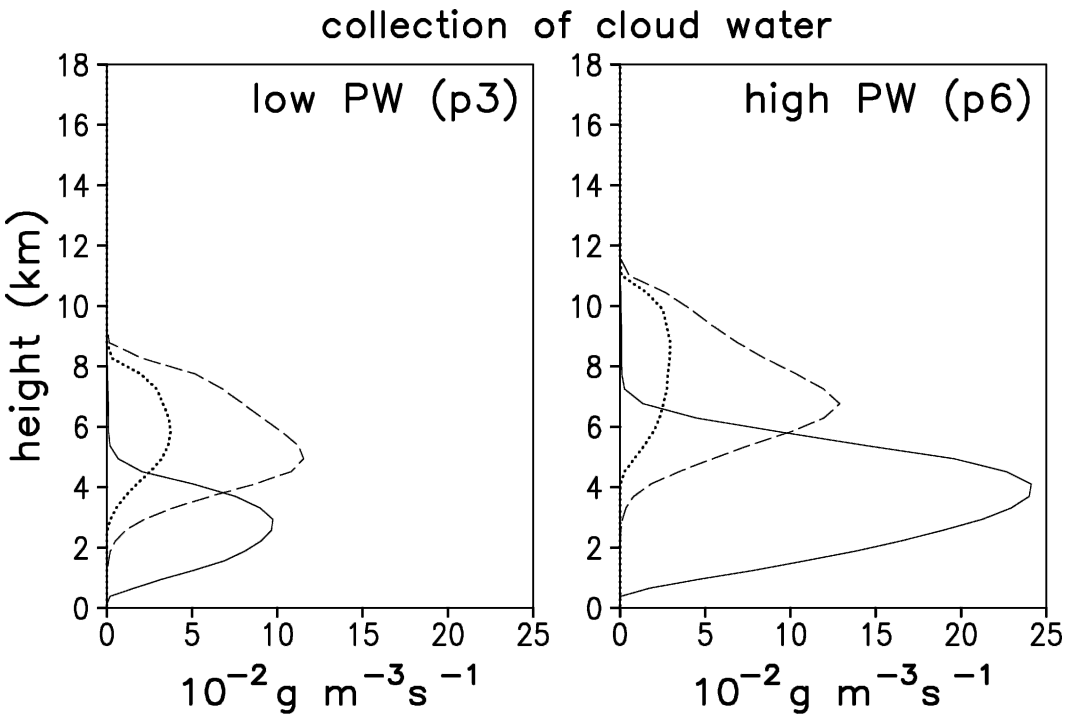

FIG. 15. Collection of cloud water by rain (solid), by hail (dashed), and by graupel (dots), (10^{-2} g m^{-3} s^{-1}) for the low-PW *e2c2m4n4k6f6p3h9* (solid) and high-PW *e2c2m4n4k6f6p6h9* (dashed) experiments, averaged over the whole domain for the second hour.

relative to what might be expected from the environmental PW.

The warmer sounding has a larger water vapor mixing ratio in the subcloud layer, and therefore has more condensation in the updrafts, more fallout of precipitation, and more evaporation of rain per unit updraft mass flux at the cloud base. This results in a larger ratio of downdraft mass flux to updraft mass flux for the warmer sounding. Also influencing the strength of the downdrafts is the fact that the greater fallout of precipitation with the warmer sounding generates greater negative buoyancy in addition to what is due to evaporative cooling. Therefore, besides producing stronger downdrafts, the warmer sounding produces downdrafts with a greater deficit in water vapor mixing ratio, relative to the initial state, than does the colder sounding (Fig. 20). This is relevant to the further production of downdrafts because for many of the simulations the rain is falling into cold outflow, not into undisturbed air. Because the cold outflow is drier in the warmer sounding, more evaporation can result.

c. *Implications for storm predictability*

The results in Fig. 7 indicate that the storms in the *p6* environments tend to generate a wider range of precipitation rates than their *p3* counterparts. Because of

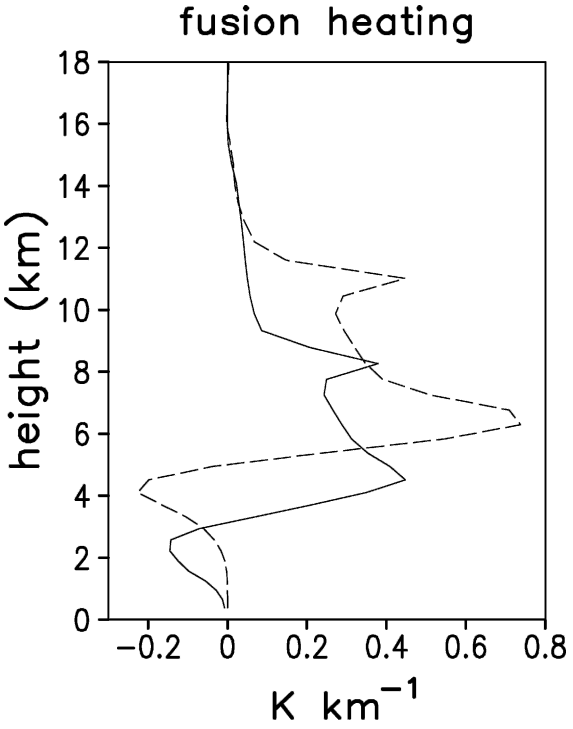

FIG. 16. Release of latent heat of fusion (K km^{-1}) in updrafts for the low-PW *e2c2m4n4k6f6p3h9* (solid) and high-PW *e2c2m4n4k6f6p6h9* (dashed) experiments, averaged over the whole domain for the second hour.

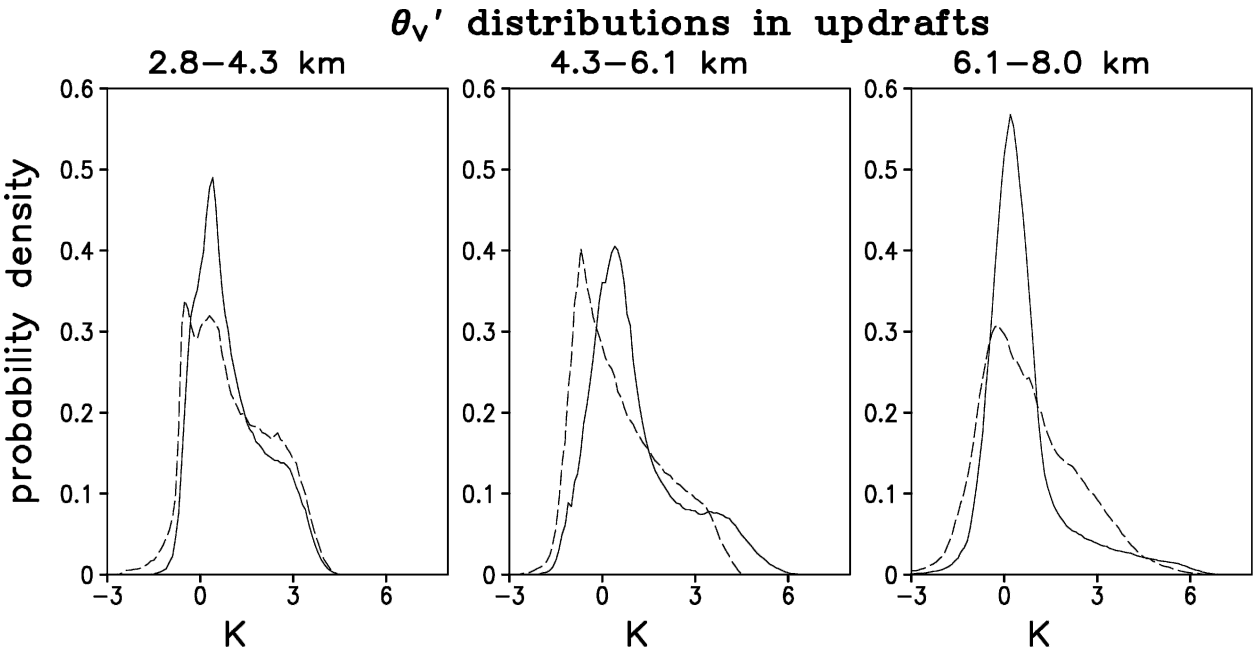

FIG. 17. Distribution of θ_v' in three different layers (see plot labels) in the updrafts for the low-PW *e2c2m4n4k6f6p3h9* (solid) and high-PW *e2c2m4n4k6f6p6h9* (dashed) experiments, averaged over the whole domain for the second hour.

the way our parameter space study is designed, these variations in precipitation rates occur for precisely the same range of environmental variations in both PW regimes, with the possible exception of CAPE, which is open to interpretation. Because of the greater sensitivity of the *p6* storms' precipitation rates to the same range of environmental variations, it appears that the warm, high-PW environments may offer less predictability than their cool, low-PW counterparts.

This apparent loss of predictability in warmer, high-PW environments may be seen partly as a consequence of the factors that produce weaker updrafts there. In fact, some of the weak shear (small *n*), weak low-level lapse-rate (small *m*) storms in the *e2c2p6* simulation series, particularly the *k2f2* subset (not shown), exhibit a tendency to dissipate during the second hour. This tendency is even more pronounced for some of the low-CAPE (*e1*) series simulations. Some of these variations might be explainable in terms of variations in reversible CAPE across the various simulations. To test this idea, we constructed a new version of our *p6* environment, featuring an amplified buoyancy profile yielding SBCAPE-RLF equal to the SBCAPE-RLF of our extant *p3* environment. This new simulation also shows the enhanced variability in surface precipitation rates shown by the earlier *p6* case, confirming our suspicion that the high-PW environments tend to be associated with reduced predictability, at least with respect to precipitation.

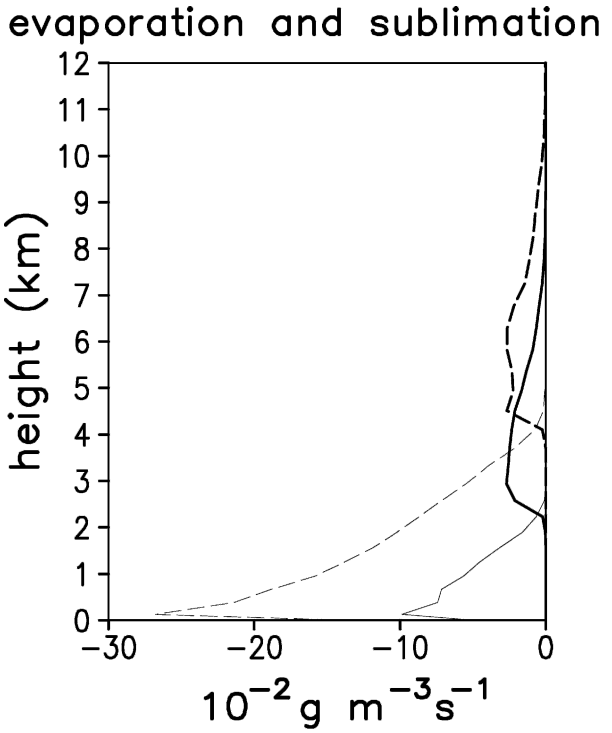

FIG. 18. Evaporation of rain (thin) and sublimation (thick) of frozen precipitation (10^{-2} g m^{-3} s^{-1}) for the low-PW *e2c2m4n4k6f6p3h9* (solid) and high-PW *e2c2m4n4k6f6p6h9* (dashed) experiments, averaged over the whole domain for the second hour.

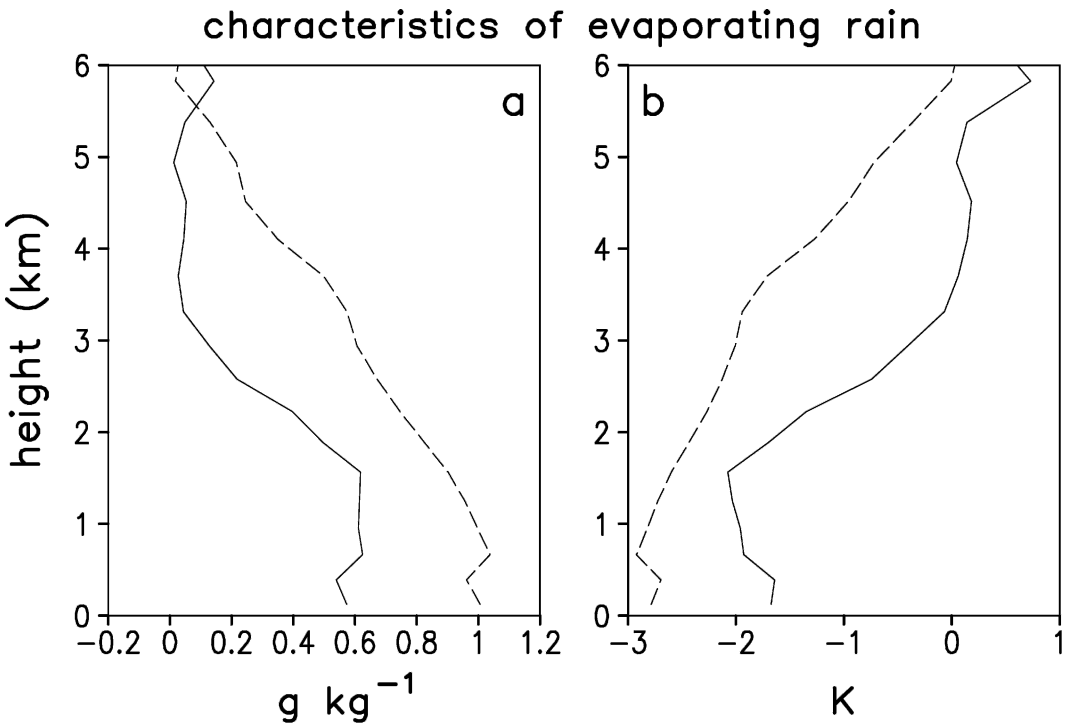

FIG. 19. (a) Saturation mixing ratio at rain temperature minus water vapor mixing ratio (g kg^{-1}), for rain that is evaporating, for the low-PW *e2c2m4n4k6f6p3h9* (solid) and high-PW *e2c2m4n4k6f6p6h9* (dashed) experiments, averaged over the whole domain for the second hour. (b) Same as in (a), but for rain temperature minus ambient air temperature (K).

From another perspective, many of the low-PW (*p3*) storms not only have stronger updrafts, but also exhibit more pronounced supercellular traits. The enhanced rotational organization of such storms has been proposed (Lilly 1986) as being associated with greater predictability. Furthermore, the *p6* simulations tend to generate more numerous updrafts than do the *p3* simulations, implying more competition for warm low-level inflow in the *p6* environments.

These findings suggest that the specification of subgrid turbulence mixing processes may also be an important factor to consider in detailed studies of predictability of storms in marginal environments. It is far from clear that numerical models provide accurate representations of convection at the lower limits of storm initiation and survivability. At those lower limits, the influence of external forcing factors other than the vertical environmental profiles may well become very important, which further complicates the situation.

d. Implications for storm intensity

We note that the PW in the cooler, low-PW (*p3*) environments studied here approximates that commonly found in severe storm cases on the Great Plains of the United States, while the PW in the warmer, high-PW (*p6*) environments is more characteristic of tropical environments. It is therefore possible that the enhanced intensity of our *p3* storms may be one factor underlying the intensity of many storms on the Great Plains, which are renowned for their severity. Of course, other factors are likely at work as well; large CAPEs and favorable vertical shears are also common in the lee of the Rocky Mountains in the spring and early summer. The relative invigoration of storms in *p3* environments may also play a role in promoting the great severity of storms seen elsewhere during the early part of spring, as compared to later in the storm season. In this case, too, other factors are also undoubtedly at work, such as stronger large-scale baroclinity and vertical shear in the early spring.

The enhanced intensity of the *p3* storms is also accompanied by stronger updraft rotation and more deviate storm motion (not shown). Current standard methods of forecasting storm motion rely solely on characteristics of the environmental wind profile (see Bunkers et al. 2000). Results from our parameter space study clearly indicate some influence on storm motion from environmental thermodynamic parameters, a subject that is currently under investigation.

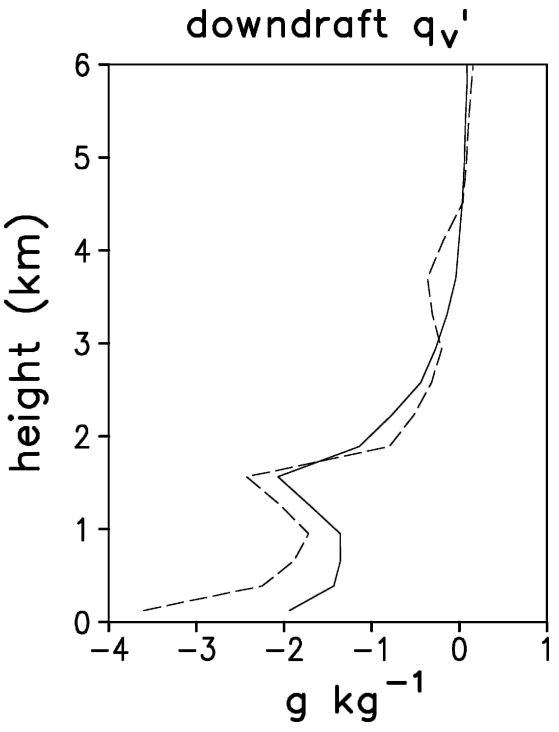

FIG. 20. Water vapor mixing ratio (g kg^{-1}) in downdrafts minus initial state for the low-PW *e2c2m4n4k6f6p3h9* (solid) and high-PW *e2c2m4n4k6f6p6h9* (dashed) experiments, averaged over the whole domain for the second hour.

While these findings may be helpful in understanding convective mode and intensity in a general sense, we urge caution in applying these findings directly to forecasting. In the real-world, storm forecasting is complicated by the strong effects of variations in other environmental parameters, the complex effects of storm triggering mechanisms, the variability of storm microphysics parameters, and the positive incidental correlation between CAPE and LCL temperatures observed in the real atmosphere.

5. Summary and future outlook

We have shown that storms in environments having cooler temperatures and smaller amounts (30 mm) of PW tend to produce stronger updrafts and almost as much surface precipitation as storms in warmer environments with twice as much PW, all other environmental parameters being held equal. The low-PW storms thus display significantly larger environmental or climatological precipitation efficiency than do their high-PW counterparts. The behavior of the low-PW storms is directly related to their stronger updrafts, which are the result of the extra positive buoyancy added by fusion processes that start at lower altitudes than in the high-PW storms, and especially of the deficit in the negative buoyancy associated with the condensate loading at low PW. The low-PW storms appear to have a higher convective overturning efficiency than the high-PW storms, but much of this can be explained by their larger reversible CAPEs. We also note that the high-PW storms tend to produce a wider range of surface precipitation rates than do the low-PW storms, suggesting some reduction of overall predictability in the warmer, moister, high-PW regime.

There appear to be many directions to follow for future research efforts. The more complex behavior and possible reduction in predictability for storms in high-PW environments suggests the need to conduct a full parameter space inquiry about the possible superiority of reversible CAPE over pseudoadiabatic CAPE in predicting updraft intensity. If reversible CAPE is shown to be consistently superior, then additional parameter space simulations using buoyancy profiles based on reversible adiabats, instead of pseudoadiabats, might yield additional new insights into the higher-order effects that influence storm dynamics. There is also a need to consider the impact on storms of variations in the free-tropospheric humidity. In addition, the varying sensitivities of the simulated storms to all the key environmental variables suggests that the predictability of storms may exhibit significant differences across many parts of the full parameter space. The considerable sensitivity of storm intensity to PW and the other environmental parameters is also accompanied by sizeable variability in storm motions as a function of these numerous parameters. Inasmuch as storm motions are currently forecast using only hodograph parameters, a quantitative study of how storm motion responds to changes in all the key environmental parameters is needed. The robustness of the present findings under variations in initiation methods and horizontal environmental inhomogeneities should also be assessed.

Acknowledgments. This research is a part of the Convection Morphology Parameter Space Study (COMPASS), which is supported by Grant ATM-0126408 from the National Science Foundation, under the supervision of Dr. Stephan Nelson. We also thank the anonymous reviewers for their many insightful comments on this manuscript. We are also grateful to Kerry Emanuel and Nilton Renno, whose CAPE programs were made available to us for the purpose of verification of our software. (For additional information on the COMPASS study, see our Web site online at http://space.hsv.usra.edu/COMPASS.) The COMPASS numerical simulations were conducted on the Matrix linux

cluster at the University of Alabama in Huntsville (UAH). We also acknowledge programming support from Jayanthi Srikishen of USRA Huntsville, and computer system support from Scott Podgorny, UAH, throughout this project.

APPENDIX

Revisions to the Cloud Model

The modifications recently incorporated into our RAMS model version include not only new initialization procedures for the experiments, but also actual changes and refinements to the model itself. For completeness, the changes relative to the methodology used in MC02 are listed as follows.

1) We employed a redesigned starting thermal bubble that includes a positive q_v perturbation that approximately conserves LCL heights within the bubble; tests indicate that use of warm bubbles having no moisture enhancement and no LCL conservation can hinder storm development in some low-LCL, high-LFC environments.
2) We repaired several errors in our experiment design and initialization procedures; one was causing relative humidities to be too small at very low temperatures; another was allowing variations of a few percent between some experiments that were supposed to have specified CAPEs; our specified SBCAPE-P values are now realized accurately to within 10 J kg^{-1} tolerance; these fixes were found to have only a minor impact on the simulations, and did not alter the basic storm structure and intensity trends within the parameter space; we also fixed other errors in our initialization procedure to increase the accuracy of our calculations of Richardson numbers used in designing the subcloud layers in our initial soundings; this latter fix has resulted in increased static stability in our subcloud layers.
3) In implementing our expanded parameter space study, which includes cases with larger hodograph radii and stronger shears, we continued to use the approach of letting the lowest Richardson number experiment dictate the "subcloud" stability for all our experiments; because we now include cases having stronger shears than in MW01 and MC02, we had to increase subcloud stability even further compared to that mentioned in the previous item. This approach to the design of the subcloud layer ensures that Richardson numbers do not become so small as to trigger spontaneous turbulent mixout of the subcloud layer in the strongest shear cases; because of this increase in the limiting allowable subcloud stability, we also redesigned our thermodynamic profiles aloft so that low-level lapse rates are not quite as large as in our previous studies; our new cases thus do not have strictly the same profile shapes as our previously published cases, but the trends noted in the earlier papers are confirmed, except for a few of the vorticity statistics, which now show clearer trends and are, we believe, more realistic; see also item 8 below.
4) We repaired a minor error in the model's autoconversion calculations, in which a factor equal to atmospheric density was erroneously omitted. This fix did not have a major impact on any of our findings, because the error was quantitatively small, and autoconversion is generally not as important as collection in the production of precipitation in mature storms.
5) We refined the model's iterative calculations of temperature from ice-liquid potential temperature, by tightening the threshold for convergence; this makes our buoyancy computations more accurate.
6) We borrowed code from later versions of RAMS to partition the amounts of hail and graupel in a way that appears more realistic; in particular, we implemented a scheme similar to Eq. (2.10) of Meyers et al. (1997), with appropriately chosen collection weighting factors for each of the hydrometeor interactions.
7) We repaired all the collection tables governing hydrometeor species interactions for all values of hydrometeor distribution shape parameter different from those used previously by us (i.e., the tables used in MC02 were already correct), so that they more closely conform to the stochastic collection integral [e.g., Eq. (46) of Walko et al. 1995]. This allows us to conduct sensitivity experiments on the impact of changes in the hydrometeor distribution shape parameter (to be reported in another paper).
8) We changed the model turbulent diffusion computations from anisotropic (IDIFFK = 2) to isotropic (IDIFFK = 3), believed to be more appropriate for these simulations, where convection is explicitly resolved on a grid that is reasonably close to unit aspect ratio. This change appears to have a beneficial impact on the vorticity statistics. We also increased the mixing length scale factor used in computing diffusion from 0.25 to 0.30; this improves solution smoothness. The minimum turbulent diffusion coefficient (see Table 2) was also raised to improve solution smoothness, in anticipation of exploration of a wider parameter space, some parts of which could generate stronger storms than those in MC02.
9) We revised the model's formulas for saturation va-

por pressure over water and ice to obtain more accurate representations than the default eighth-order polynomial approximation. We now use the exact Clausius–Clapeyron integral given by Lipps and Hemler (1980) over water, and Tetens formula over ice (see Bolton 1980); for consistency, we also used these same expressions in our environmental profile design algorithm.

REFERENCES

Bolton, D., 1980: The computation of equivalent potential temperature. *Mon. Wea. Rev.,* **108,** 1046–1053.

Bryan, G. H., and J. M. Fritsch, 2004: A reevaluation of ice-liquid water potential temperature. *Mon. Wea. Rev.,* **132,** 2421–2431.

——, J. C. Wyngaard, and J. M. Fritsch, 2003: Resolution requirements for the simulation of deep moist convection. *Mon. Wea. Rev.,* **131,** 2394–2416.

Bunkers, M. J., B. A. Klimowski, J. W. Zeitler, R. L. Thompson, and M. L. Weisman, 2000: Predicting supercell motion using a new hodograph technique. *Wea. Forecasting,* **15,** 61–79.

Cotton, W. R., and R. A. Anthes, 1989: *Storm and Cloud Dynamics.* Academic Press, 883 pp.

Doswell, C. A., H. E. Brooks, and R. A. Maddox, 1996: Flash flood forecasting: An ingredients-based methodology. *Wea. Forecasting,* **11,** 560–581.

Emanuel, K. A., 1994: *Atmospheric Convection*. Oxford University Press, 580 pp.

Fankhauser, J. C., 1988: Estimates of thunderstorm precipitation efficiency from field measurements in CCOPE. *Mon. Wea. Rev.,* **116,** 663–684.

Ferrier, B. S., J. Simpson, and W.-K. Tao, 1996: Factors responsible for precipitation efficiencies in midlatitude and tropical squall simulations. *Mon. Wea. Rev.,* **124,** 2100–2125.

Klemp, J. B., and R. B. Wilhelmson, 1978: The simulation of three-dimensional convective storm dynamics. *J. Atmos. Sci.,* **35,** 1070–1096.

Li, Y., S. Gao, and J. Liu, 2004: Assessment of several moist adiabatic processes associated with convective energy calculation. *Adv. Atmos. Sci.,* **21,** 941–950.

Lilly, D. K., 1962: On the numerical simulation of buoyant convection. *Tellus,* **14,** 148–172.

——, 1986: The structure, energetics and propagation of rotating convective storms. Part II: Helicity and storm stabilization. *J. Atmos. Sci.,* **43,** 126–140.

Lipps, F. B., and R. S. Hemler, 1980: Another look at the thermodynamic equation for deep convection. *Mon. Wea. Rev.,* **108,** 78–84.

Manzato, A., and G. Morgan Jr., 2003: Evaluating the sounding instability with the Lifted Parcel Theory. *Atmos. Res.,* **67–68,** 455–473.

Market, P., S. Allen, R. Scofield, R. Kuligowski, and A. Gruber, 2003: Precipitation efficiency of warm-season Midwestern mesoscale convective systems. *Wea. Forecasting,* **18,** 1273–1285.

McCaul, E. W., Jr., and M. L. Weisman, 1996: Simulations of shallow supercell storms in landfalling hurricane environments. *Mon. Wea. Rev.,* **124,** 408–429.

——, and ——, 2001: The sensitivity of simulated supercell structure and intensity to variations in the shapes of environmental buoyancy and shear profiles. *Mon. Wea. Rev.,* **129,** 664–687.

——, and C. Cohen, 2002: The impact on simulated storm structure and intensity of variations in the mixed layer and moist layer depths. *Mon. Wea. Rev.,* **130,** 1722–1748.

Meyers, M. P., R. L. Walko, J. Y. Harrington, and W. R. Cotton, 1997: New RAMS cloud microphysics parameterization. Part II: The two-moment scheme. *Atmos. Res.,* **45,** 3–39.

Pielke, R. A., and Coauthors, 1992: A comprehensive meteorological modeling system—RAMS. *Meteor. Atmos. Phys.,* **49,** 69–91.

Smagorinsky, J., 1963: General circulation experiments with the primitive equations. Part I: The basic experiment. *Mon. Wea. Rev.,* **91,** 99–164.

Tripoli, G. J., and W. R. Cotton, 1981: The use of ice-liquid water potential temperature as a thermodynamic variable in deep atmospheric models. *Mon. Wea. Rev.,* **109,** 1094–1102.

——, and ——, 1982: The Colorado State University three-dimensional cloud/mesoscale model—1982. Part I: General theoretical framework and sensitivity experiments. *J. Rech. Atmos.,* **16,** 185–219.

Walko, R. L., W. R. Cotton, M. P. Meyers, and J. Y. Harrington, 1995: New RAMS cloud microphysics parameterization. Part I: The single-moment scheme. *Atmos. Res.,* **38,** 29–62.

Weisman, M. L., and J. B. Klemp, 1982: The dependence of numerically simulated convective storms on vertical wind shear and buoyancy. *Mon. Wea. Rev.,* **110,** 504–520.

——, and ——, 1984: The structure and classification of numerically simulated convective storms in directionally varying shears. *Mon. Wea. Rev.,* **112,** 2479–2498.

Williams, E., and N. Renno, 1993: An analysis of the conditional instability of the tropical atmosphere. *Mon. Wea. Rev.,* **121,** 21–36.

——, and S. Stanfill, 2002: The physical origin of the land-ocean contrast in lightning activity. *C. R. Physique,* **3,** 1277–1292.

Willoughby, H. E., D. P. Jorgensen, R. A. Black, and S. L. Rosenthal, 1985: Project STORMFURY: A scientific chronicle. *Bull. Amer. Meteor. Soc.,* **66,** 505–514.

Zipser, E. J., and M. A. LeMone, 1980: Cumulonimbus vertical velocity events in GATE. Part II: Synthesis and model core structure. *J. Atmos. Sci.,* **37,** 2458–2469.